Distribution Agreement

Signature:

__________________________ ___________

Alexander John Poplawsky Date

Direct Detection of Neural Magnetic Fields with Fast-Temporal Resolution Magnetic Resonance Spectroscopy

By

Alexander John Poplawsky
Doctor of Philosophy

Graduate Division of Biological and Biomedical Science
Neuroscience

Xiaoping Hu, Ph.D.
Advisor

Raymond Dingledine, Ph.D.
Committee Member

George Andrew James, Ph.D.
Committee Member

Shella Keilholz, Ph.D.
Committee Member

Krishnankutty Sathian, M.D., Ph.D.
Committee Member

Accepted:

Lisa A. Tedesco, Ph.D.
Dean of the James T. Laney School of Graduate Studies

Date

Direct Detection of Neural Magnetic Fields with Fast-Temporal Resolution Magnetic Resonance Spectroscopy

By

Alexander John Poplawsky
B.S., University of Pittsburgh, 2004

Advisor: Xiaoping Hu, Ph.D.

An abstract of
A dissertation submitted to the Faculty of the
James T. Laney School of Graduate Studies of Emory University
in partial fulfillment of the requirements for the degree of
Doctor of Philosophy
in the Graduate Division of Biological and Biomedical Science
Neuroscience
2011

ABSTRACT

Direct Detection of Neural Magnetic Fields with Fast-Temporal Resolution
Magnetic Resonance Spectroscopy
By Alexander John Poplawsky

Functional magnetic resonance imaging (fMRI) indirectly detects brain activation by measuring the hemodynamic response to increased energy demand. The detection of neural magnetic fields (NMFs) with MRI seeks to improve the temporal and spatial accuracy of fMRI by directly measuring the electrical responses of the brain. *In vivo* studies of the human brain provide conflicting results for the true detection of NMFs and are hypothesized to be contaminated by signal changes originating from the blood. Our experiments are the first to measure axonal NMFs by examining the free-induction decay (FID) at a sub-millisecond temporal resolution. Two *in vitro* preparations were chosen to eliminate confounding signal changes attributed to the vasculature and simultaneous field potential recording was used to time-lock neural activity to the onset of the FID. In the first study, we experimentally measured an FID phase change associated with a single evoked action potential from the earthworm giant axon system. A maximum phase change of $[-1.2 \pm 0.3] \times 10^{-5}$ radians was observed in the background-subtracted FID. In addition, the experimental phase time course correlated well with a theoretical phase time course in both amplitude and temporal characteristics. In this way, this study provides the first evidence for the direct detection of a magnetic field from an evoked action potential using magnetic resonance technology. In the second study, we determined that the signal changes associated with evoked CA1 neurons of the rat hippocampal slice were 25 to 100 times below our detection limits. Theoretical simulations and experimental measurements support that our methods are sensitive to axonal components of the evoked NMF and insensitive to dendritic components. In this way, our technique measures signal changes originating from the white matter, unlike current fMRI techniques that measure signal changes originating from the gray matter.

Direct Detection of Neural Magnetic Fields with Fast-Temporal Resolution Magnetic Resonance Spectroscopy

By

Alexander John Poplawsky
B.S., University of Pittsburgh, 2004

Advisor: Xiaoping Hu, Ph.D.

A dissertation submitted to the Faculty of the
James T. Laney School of Graduate Studies of Emory University
in partial fulfillment of the requirements for the degree of
Doctor of Philosophy
in the Graduate Division of Biological and Biomedical Science
Neuroscience
2011

ACKNOWLEDGMENTS

Graduate school would have been much more difficulty, if not impossible, without the many people who surrounded and supported me. To them, I would like to dedicate this manuscript as it belongs to them as much as it belongs to me.

First, I would like to thank my advisor, Xiaoping Hu, who gave me the freedom and courage to pursue such a difficult, but rewarding, project. At times, I would become frustrated with the amount of time invested in developing our new technique, only to find negative results at the end. Thank you for your support during those times and trusting that there was something great around the corner.

Next, to my committee member (and unofficial advisor), Ray Dingledine. Thank you for opening your doors and accepting me as one of your own lab members. Not only did your guidance provide the key element of "simultaneous electrophysiology" to our experiments, but you opened my mind to a new way of thinking about this project. Without you and Geidy Serrano, the earthworm experiment would have never had legs.

To my other committee members, Andy James, Shella Keilholz and Krish Sathian. Your advice always cleared my vision and your encouragement allowed me to keep a confident attitude toward my goals.

To all the others at the BITC, Ray's lab and the Neuroscience class of 2005, thank you for your friendship and good times. Without you, I would have prematurely gone crazy in my mid- to late-twenties instead of my golden years. You are all the best and I thank you for being there with me.

Finally, I would have never arrived here at Emory or completed this voyage without my family. Mom and Dad, thank you for giving me your good genes. I see and hear both of you every day and I am forever grateful to have both of you as my inspiration. Jon, we have been brothers and best friends for as long as we were together. Your excitement for life is infectious and has me always looking up to you. Lastly, to my lovely wife, Megan. You have brought so much color and fun to my life with your endless passion and your goofy humor. But mostly, you were my motivation for getting the hell out of here. I don't know who I would be without you.

TABLE OF CONTENTS

CHAPTER 1: General Introduction

CHAPTER 2: The Direct Detection of a Single Evoked Action Potential with Magnetic Resonance Spectroscopy in *Lumbricus Terrestris*

CHAPTER 3: Examining the Direct Detection of Evoked Potentials in the CA1 Region of the Rat Hippocampus with Magnetic Resonance Spectroscopy

CHAPTER 4: Conclusions and Future Directions

List of Figures

CHAPTER 1: General Introduction

CHAPTER 2: The Direct Detection of a Single Evoked Action Potential with Magnetic Resonance Spectroscopy in *Lumbricus Terrestris*

CHAPTER 3: Examining the Direct Detection Of Evoked Potentials in the CA1 Region of the Rat Hippocampus with Magnetic Resonance Spectroscopy

CHAPTER 1

General Introduction

1-1 Introduction

Functional magnetic resonance imaging (fMRI) is a popular non-invasive technique used to study *in vivo* neural activity. However, fMRI measures signal changes associated with the hemodynamic response to increased metabolic demands of activated tissue and is not a direct measure of the electrical activity of neurons (Ogawa, Lee et al. 1990; Jezzard, Matthews et al. 2001). As a consequence, the temporal resolution of fMRI is limited to seconds as the onset of the hemodynamic response is delayed and long outlasts neural activity (Ernst and Hennig 1994; Buxton and Frank 1997). The localization of the neural activity is also inaccurate as fMRI measures signal changes from the vasculature and not from the activated neural tissue. Lastly, researchers do not fully understand the complete mechanism of how the hemodynamic response couples to neural activity, and prohibits precise quantitative assessments of brain function. The direct detection of neural magnetic fields (NMFs) with MRI will allow for the accurate measurement of neural activity in both time and space, while facilitating quantitative measurements in functional imaging studies.

The detection of transient magnetic fields with magnetic resonance (MR) technology and the challenges associated with their discovery is reviewed (see, Hagberg, Bianciardi et al. 2006; Jasanoff 2007). Initial theoretical experiments outline and successfully demonstrate detection of magnetic fields in water phantoms that conduct currents at physiological magnitudes (Bodurka and Bandettini 2002; Konn, Gowland et al. 2003; Pell, Abbott et al. 2006). Further computational modeling provides insight into the mechanism of NMF detection and predicts expected MR signal changes that can be measured (Xue, Gao et al.

2006; Blagoev, Mihaila et al. 2007; Park and Lee 2007; Cassarà, Hagberg et al. 2008). On the contrary, *in vivo* studies of the human brain do not arrive at a consensus on the detectability of the NMF signal. Signal from fast components of the hemodynamic response are hypothesized to contaminate the NMF signal and leads to different results. In addition, the NMF is faster than the relatively slow temporal resolution of MRI (tens of ms) and may be too slow to measure any signal changes attributed to the NMF (Xiong, Fox et al. 2003; Bianciardi, Di Russo et al. 2004; Chu, de Zwart et al. 2004; Konn, Leach et al. 2004; Liston, Salek-Haddadi et al. 2004; Parkes, de Lange et al. 2007). *In vitro* studies that physically decouple the NMF from the vascular system have reported convincing evidence for NMF detection in physiological systems, but do not remedy the time resolution limit of MRI (Park, Lee et al. 2004; Park, Lee et al. 2006; Petridou, Plenz et al. 2006). In the following studies, sub-microsecond time resolution magnetic resonance spectroscopy (MRS) (Ernst and Hennig 1994) is examined as a method to resolve the temporal signature of the NMF *in vitro*.

1-2 Magnetic Resonance Spectroscopy Physics and Theory of Neural Magnetic Field Detection

The abundance of water hydrogen protons and their magnetic properties are the focus of the signal measured by MRS. The proton has a non-zero magnetic moment as a result of its positive charge spinning about its axis. When exposed to a static magnetic field (B_0), the direction of the proton magnetic moment spontaneously aligns with B_0 and simultaneously precesses about B_0 with a specific frequency $f = \gamma B_0$ (f = resonant or Larmour frequency, γ = proton gyromagntic ratio). Next, a second transient magnetic field is applied perpendicular to B_0 at the Larmour frequency (B_1), which causes the proton magnetic moments to align with it. B_1 is then turned off and the magnetic moments once again precess at the Larmour frequency around B_0, but in a plane perpendicular to B_0. A receive coil, precisely tuned to the Larmour frequency, measures the electromotive force (emf) or current induction generated by this precession. The induction at the receiver naturally decays in time as the proton magnetic moments relax to equilibrium along B_0 (T_1 relaxation) and from dephasing due to interactions among other magnetic moments (T_2 relaxation). The induction of current in the receive coil caused by the hydrogen magnetic moments that decreases in time as the signal returns to equilibrium is referred to as the free-induction decay (FID) (Haacke, Brown et al. 1999).

A transient NMF creates a local magnetic field inhomogeneity that perturbs the signal generated by the protons. When a current pulse is transmitted through a conductor, a magnetic field gradient (a field inhomogeneity) is generated perpendicular to the electric field. The component of this gradient that is parallel to the static magnetic field (B_0) and is present after B_1 will constructively or destructively interfere with B_0 and change the total magnetic field experienced by a proton (B_T). This will result in a shift in the phase of the signal (due to a proton population experiencing the same B_T) and a decrease in the magnitude of the signal (due to a proton population experiencing a different magnitude of the B_T gradient) (Bodurka and Bandettini 2002). Specifically, the latter phenomenon is conventionally described as an increase in the rate of the transverse relaxation constant due to magnetic field inhomogeneities (T_2*

relaxation). A T_2*-weighted image exploits the signal magnitude loss due to field inhomogeneities in order to provide image contrast (Haacke, Brown et al. 1999).

1-3 Magnetoencephalography

Original theories regarding the detection of the NMF with MRI assume many of the conclusions originating from magnetoencephalography (MEG) studies. These main assumptions are analyzed with specific attention paid to the differences between these two modalities in detecting the NMF. Magnetic fields generated by a single neuron can be separated into dendritic and axonal NMF components. First, the membrane potential of an action potential is initially depolarized by inward Na^+ current and is soon repolarized by outward K^+ currents. The NMF generated by this type of current is modeled as two current dipoles oppositely oriented and termed a quadrapole. A quadrapole has a magnetic field that decays proportional to r^{-3} (r = distance from the magnetic field source) and is generally ignored as a possible source of NMF detection for MEG (Hämäläinen, Hari et al. 1993) and MRI (Xue, Gao et al. 2006; Blagoev, Mihaila et al. 2007; Park and Lee 2007). On the contrary, the NMF associated with the dendrite is a single post-synaptic event that is either depolarizing or hyperpolarizing in nature. This type of event often has a net current flowing in a single direction at any moment in time and, therefore, is modeled as a dipole. The magnetic field of a dipole decays proportional to r^{-2} and is considered the only source of the detectible neuronal NMF for MEG (Hämäläinen, Hari et al. 1993) and MRI (Xue, Gao et al. 2006; Blagoev, Mihaila et al. 2007; Park and Lee 2007).

The conclusion that the dendrite is the only source of detectable magnetic fields is valid for MEG, but is questionable for MR methods. The magnetic field measured by MEG is detected at a large distance from its source (r = 2-4 cm). At this large distance, it can be understood that the dendritic NMF (r^{-2}) will outweigh the axonal NMF (r^{-3}). However, MRI measures a signal generated by water protons at the source of the NMF (Chow, Cook et al. 2006; Chow, Cook et al. 2006; Chow, Cook et al. 2007) and is, therefore, synonymous with magnetic source MRI. If a magnetic source MRI voxel size is 1 mm^3, then the signal contributed by the axonal NMF is not nearly as decayed as in MEG. Also, the current amplitudes of the action potential are much larger than that of the post-synaptic potential and result in a larger magnetic field originating from the axon. Both of these considerations warrant further investigation into the individual contributions of axons and dendrites to NMF detection.

The NMF of a dendrite or axon can originate from intracellular, extracellular and membrane current sources. Computational modeling (Swinney and John P. Wikswo 1980; Roth and Wikswo 1985; Wikswo 1989; Blagoev, Mihaila et al. 2007) and experimental measurements (Roth and Wikswo 1985; Okada, Wu et al. 1997) of magnetic fields provide evidence that the detected NMF is determined mostly by the intracellular current and insignificantly by the extracellular and membrane currents. In this way, the NMF detected by MR technology will reflect intracellular current recordings without the need to puncture the cell membrane.

1-4 Phantom Models

Transient magnetic fields comparable to NMFs are successfully detected in water phantom studies. A phantom contains a wire conductor suspended in water and is electrically linked to a pulse generator that delivers a synchronized stimulus during MRI data acquisition. To date, transient magnetic fields of specified strength and duration were detected using phase imaging, 0.20 nT for 40 ms (Bodurka and Bandettini 2002) and 0.11 nT for 35 ms (Konn, Gowland et al. 2003), and magnitude imaging, 0.44 nT for 20 ms (Pell, Abbott et al. 2006). The strength of *in vivo* NMFs were measured by MEG and determined to have a strength of ~10 pT for spontaneous neuronal activity and ~1 pT for evoked activity 2-4 cm from the source, which is calculated to be 0.1 – 1.0 nT at the NMF source (Bodurka and Bandettini 2002). Therefore, the results of the phantom studies provide a lower limit of transient magnetic field detection that is within the range of physiological NMFs.

A great advantage of phantom studies is the use of time-locked stimuli to greatly increase the sensitivity in detecting small signal changes through temporal averaging. Although phantom studies offer a good initial approach in detecting transient magnetic fields, their simplistic dipolar construction do not offer complete insight into the realistic detection of the more complex NMF. In addition, the magnetic susceptibility difference between the metal conductor and the water medium of the phantom enhances the detection of small magnetic fields (Huang, Posnansky et al. 2006). Such enhancements will not be present in living tissue as the magnetic susceptibility of water and neurons are similar.

1-5 Computer Modeling

Computer modeling is a useful tool in predicting the nature of NMF detection and these simulations suggest that some assumptions adopted from MEG may not apply to magnetic source MRI. Xue and colleagues (2006) modeled the neuron as a multi-dipole and concluded that NMFs were generated solely in cortical dendrites and that they could only be detected with magnitude imaging (2% change). In addition, Park and Lee (2007) modeled the dendrite and axon separately to determine their independent contributions to the NMF signal change. The dendrite was modeled as a dipole and a phase change of 0.14^{o} with no detectable magnitude change was calculated. The axon model was represented as a quadrapole and an insignificant signal contribution was concluded if the entire action potential occurred within an echo time of 10 ms. This model does not consider the signal change with a time resolution less than 10 ms nor a large population of axons that synchronously fire. This latter inconsideration may account for claims of positively detecting NMFs in the human optic nerve (Chow, Cook et al. 2006; Chow, Cook et al. 2006) and corpus callosum (Chow, Cook et al. 2007) where the NMFs constructively interfere.

To better represent NMFs of a living neuron, Blagoev and colleagues (2007) designed their model after a single cortical pyramidal neuron of the macaque. From this model, the NMF was a dipole several centimeters away from the source, as in MEG, but substantially differs from a dipole at its source. The contributions of the extra- and intracellular currents to the NMF were also analyzed in the neuron model. The extracellular current was calculated to contribute ~10^{-6} times that of the intracellular current in both phase and magnitude imaging. They concluded a 1.6% magnitude and a 1^o phase change in the MR signal that originated mostly from the intracellular current.

In a more recent study, Cassarà and colleagues (2008) calculated the NMFs that originated from a 1.7 mm^3 volume of simulated CA1 neurons from the rat hippocampus and estimated their effects on the MR signal. The simulated neurons were digital reconstructions of real CA1 neurons that received AMPA-like excitation at the oblique dendrites as if receiving input from the Schaffer collaterals. The evoked NMFs from this CA1 volume had a mix of magnetic fields from both the axons and dendrites. The MR magnitude change was estimated to be $-\Delta 3 \times 10^{-7}$ (normalized units), which is nearly 100-times less than the estimated phase change of $\Delta 200 \times 10^{-7}$ radians (T_E = 20 ms). Heller et al. (2009) also estimated a phase change that was 100 times greater than the magnitude change. Recent studies suggest that a greater change occurs in the MR phase rather than the magnitude in response to NMFs and methods that can measure the phase component of the MR signal are necessary.

1-6 Human Studies

Magnetic source MRI in the human brain has lead to conflicting conclusions on the practicality of NMF detection *in vivo*. The main argument for discrepancies in the human brain is the existence of the hemodynamic response, which has a similar T_2* effect on the MR signal and may be a source of false positive detection.

The hemodynamic response is the combined change in blood flow, blood volume and oxygen metabolism that is coupled to neural activity and is commonly referred to as blood oxygenation level-dependent (BOLD) signal (Ogawa, Lee et al. 1990). Less than 1 s after activation, energy depleted cells begin to sequester oxygen from the vasculature by the conversion of the diamagnetic oxyhemoglobin to the paramagnetic deoxyhemoglobin (Malonek, Dirnagl et al. 1997). This local increase in deoxyhemoglobin relative to baseline creates a stronger local magnetic field gradient that dephases the precessing protons and results in a decrease in the signal magnitude (decreased T_2*) (Ernst and Hennig 1994). Next, 2-5 s after neuronal activation, an overcompensating local increase in blood flow decreases the concentration of deoxyhemoglobin to below that of baseline (Malonek, Dirnagl et al. 1997). The MR signal experiences less dephasing effects and results in an increased T_2* (Buxton and Frank 1997). The BOLD signal finally returns to baseline 12-18 s after stimulation (Jezzard, Matthews et al. 2001). Signal changes originating from the hemodynamic response could be incorrectly interpreted as NMF detection due to the disruption of T_2* by both processes.

Magnetic source MRI in humans is controversial due to the lack of evidence supporting the complete separation of the hemodynamic response and NMF. Many attempts have been made, but a lack of consensus regarding the proper method has resulted in ambiguity on whether the NMF has been detected (Fig. 1-1). The inherent low temporal resolution of MRI (~50-100 ms) may be one aspect to blame for not resolving the faster NMF from the slow hemodynamic response. MRS has a sub-millisecond temporal resolution and is considered in our studies as an alternative method to clearly elucidate the mechanism of NMF detection with MR technology.

1-7 *In Vitro* Studies

More recent studies have separated the hemodynamic response from the NMF by removing the vascular system and have revealed new evidence for the positive detection of the NMF by MRI. Park and colleagues (2004) reported a -5.49 ± 1.94% MRI magnitude change in dissected snail ganglia undergoing spontaneous activity after application of nitric oxide. The same group later reported a -2.97 ± 1.10% magnitude change in the snail ganglia following evoked activity (Park, Lee et al. 2006). However, the reported magnitude changes are 10 times larger than that expected in humans and no phase change analysis was performed, which brings question to their conclusions. However, Petridou and colleagues (2006) addressed these concerns in organotypic rat cortical cultures that are in a natural state of spontaneous electrical activity. Tetrodotoxin was added to the culture medium to block NMF generation for comparison. They report a ~0.15 – 3^{o} phase change and a 0.01 – 0.4% magnitude change at 7 T, which corresponds to an NMF of similar magnitude as is predicted by MEG studies (~0.2 – 3.9 nT). Luo and colleagues (2009) failed to indentify MR signal changes that resulted from evoked activity in the visual cortex of the bloodless turtle brain. Signal changes below 0.1% in the MR magnitude and 0.1^{o} in the MR phase were not examined in this experiment (Luo, Liu et al. 2007). The NMF associated with evoked activity is approximately 10 times less than spontaneous activity and may affect the MR signal less than the detection limits set in the bloodless turtle brain. *In vitro* MRI studies provide evidence that NMFs can be detected in biological tissue but provide little insight into how these methods can be implemented *in vivo*.

1-8 Summary

The detection of NMFs by MRI is a direct measure of brain activation and can improve the timing and location accuracy of neural activity compared to BOLD fMRI. The hemodynamic response is a poorly understood and inconsistent process that is a qualitative measure of neural activity. However, the direct detection of NMFs can include quantitative analysis of neural activity. In addition, the temporal resolution is no longer limited to the slow dynamics of the hemodynamic response, which allows the experimenter to measure at the same resolution as the neural event. In this way, functional imaging experiments will be more meaningful since the signal measured is directly related to neural activity rather than through a correlation with the hemodynamic response.

Mounting evidence from computational modeling, water phantom and *in vitro* studies provide good evidence for the positive detection of NMFs at the physiological ranges determined by MEG. Unfortunately, much controversy accompanies magnetic source MRI in human subjects due to the incomplete dissociation of the NMF from the hemodynamic response. The faster temporal resolution of MRS will be utilized in the following studies to examine the temporal signature of evoked NMFs.

Reference	T_E (ms)	T_R (s)	B_o (T)	ROI	NMF Type	Magnitude Change	Phase Change
(Xiong, Fox et al. 2003)	100	1.0	1.9	V1, M1, S1	Evoked	-1.1 ± 0.5%	-
(Chu, de Zwart et al. 2004)	40	1.0	3.0	V1	Evoked	NS	NS
(Bianciardi, Di Russo et al. 2004)	~50	1.3	1.5	V1	Evoked	t~3.35	NS
(Parkes, de Lange et al. 2007)	30, 60, 90	1.0	1.5	V1, M1	Evoked	-	NS
“	50	1.05	1.5	V1	Evoked	-	NS
(Konn, Leach et al. 2004)	24	0.04	3.0	V1	Evoked	-	NS
“	24	0.04	3.0	Whole Brain	Spont	-	$p<0.05$
(Liston, Salek-Haddadi et al. 2004)	40	3.0	1.5	Whole Brain	Spont	-3 ± 1%	-

Figure 1-1 Summary of *In Vivo* Studies: The results of MRI studies in humans depend on the sequence protocol and the experimental paradigm used. With no two studies being alike and all studies claiming to successfully separate the hemodynamic response and NMF, no general conclusion on the feasibility of NMF detection in humans can be made. Region of Interest (ROI), Spontaneous (Spont), not significant (NS), primary visual cortex (V1), primary motor cortex (M1) and primary sensory cortex (S1).

CHAPTER 2

The Direct Detection of a Single Evoked Action Potential with Magnetic Resonance Spectroscopy in *Lumbricus Terrestris*

This chapter presents work to be published as: Poplawsky A, Dingledine R and Hu X. *The Direct Detection of a Single Evoked Action Potential with Magnetic Resonance Spectroscopy in Lumbricus Terrestris*. NMR Biomed, Submitted.

2-1 Abstract

Functional magnetic resonance imaging (fMRI) indirectly measures neural activity by detecting the signal change associated with the hemodynamic response following brain activation. In order to alleviate the temporal and spatial specificity problems associated with fMRI, a number of attempts have been made to detect neural magnetic fields (NMFs) with MRI directly, but have thus far provided conflicting results. In the present study, we used magnetic resonance to detect axonal NMFs in the median giant fiber of the earthworm, *Lumbricus terrestris*, by examining the free-induction decay (FID) with a sampling interval of 0.32 ms. The earthworm nerve cords were isolated from the vasculature and stimulated at the threshold of action potential generation. FIDs were acquired shortly after the stimulation and simultaneous field potential recordings identified the presence or absence of single evoked action potentials. FIDs acquired when the stimulus did not evoke an action potential were summed as background. The phase of the background-subtracted FID exhibited a systematic change, with a peak phase difference of $[-1.2 \pm 0.3] \times 10^{-5}$ radians occurring at a time corresponding to the timing of the action potential. In addition, we calculated the possible changes in the FID magnitude and phase due to a simulated action potential using a volume conductor model. The measured phase difference matched the theoretical prediction well in both amplitude and temporal characteristics. This study provides the first evidence for the direct detection of a magnetic field from an evoked action potential using magnetic resonance.

2-2 Introduction

fMRI is a widely used technique for investigating *in vivo* neural activation by indirectly measuring signal changes that arise from the hemodynamic response due to increased metabolic demand. This hemodynamic response lacks spatial specificity as it is localized to the vasculature near the neural activity rather than the neural activity itself and does not have sufficient temporal resolution to provide the timing of the neuronal event. A direct measure NMFs with magnetic resonance (MR) can, in principal, provide a more spatially and temporally accurate measurement of brain function and has been the goal of a number of recent efforts.

Investigators initially detected transient magnetic fields using MRI in water phantoms that conducted currents at physiological magnitudes (Bodurka and Bandettini 2002; Konn, Gowland et al. 2003; Pell, Abbott et al. 2006). Computational modeling predicted the MRI signal change due to NMFs to be much smaller than the signal change attributed to the hemodynamic response (Xue, Gao et al. 2006; Blagoev, Mihaila et al. 2007; Park and Lee 2007; Cassarà, Hagberg et al. 2008). *In vivo* studies in human subjects had contradicting results on the detection of the NMF (Xiong, Fox et al. 2003; Bianciardi, Di Russo et al. 2004; Chu, de Zwart et al. 2004; Konn, Leach et al. 2004; Liston, Salek-Haddadi et al. 2004; Chow, Cook et al. 2006; Chow, Cook et al. 2006; Parkes, de Lange et al. 2007; Chow, Dagens et al. 2008). One likely reason was that the change associated with *in vivo* neural activity could not be completely separated from the hemodynamic response. *In vitro* studies that physically decoupled the neural tissue from the vascular system successfully detected NMFs that appeared to be associated with increased neural activity (Park, Lee et al. 2004; Park, Lee et al. 2006; Petridou, Plenz et al. 2006), with the exception of a recent study in the isolated turtle brain (Luo, Lu et al. 2009). However, no study has examined the effect of an evoked NMF using an MR method with a temporal resolution that is sufficient to capture the evolution of an action potential. The aim of the current study is to provide definitive experimental evidence for the direct detection of an evoked NMF using fast temporal resolution magnetic resonance spectroscopy (MRS).

We chose the median giant fiber system of the earthworm, *Lumbricus terrestris*, for the following reasons: First, the removal of the nerve cord from the vascular system is possible. Second, the two major giant axons contained in the ventral nerve cord have been well described in terms of their anatomy and electrophysiology (Bullock 1965). The lateral giant fibers (LGF) are two electrically coupled axons that function as a single unit. The median giant fiber (MGF) is a single, larger diameter axon that is located between the two lateral fibers (Fig. 2-1) and was the focus of the current study. Both fiber systems are physiologically involved in the rapid shortening reflex of the earthworm body (Rushton 1946), and activity of axon and muscle potential changes can be identified using extracellular recordings (Roberts 1962; Drewes, Landa et al. 1978; Drewes 1984). The MGF and LGF are pseudo-myelinated and ion flux across the axon membrane is concentrated to opening of the myelin at the dorsal nodes (MGF) and ventral collateral openings (MGF and LGF) (Gunther 1976). Third, it is possible to evoke a single action potential from the MGF that is uncomplicated by any other event. This includes activity of the LGF, which has a higher threshold of activation and, therefore, can remain quiescent during MGF action potential generation. Finally, action potentials can be elicited from the isolated nerve cord at room temperature and the preparation does not require oxygen gas perfusion. The latter attribute reduces concerns with paramagnetic oxygen affecting the MR signal (Luo, Liu et al. 2007).

A previous study employed a volume conductor model and predicted the magnetic field generated by a single evoked action potential from the measured intracellular potential (Woosley, Roth et al. 1985). Furthermore, Roth and Wikswo experimentally verified this model by directly measuring the magnetic field using a toroid pickup coil. They measured a Δ300 pT magnetic field from the giant axon system of the crayfish (Roth and Wikswo 1985), which is physiologically similar to the earthworm giant axon system. Likewise, a Δ300 pT magnetic field was within the range detected in water phantoms (Bodurka and Bandettini 2002; Konn, Gowland et al. 2003) and gives confidence that the earthworm action potential will be above detection threshold for our methods.

Simultaneous field potential recordings and MRS were performed to measure the voltage and magnetic field associated with a single evoked action potential. Spectroscopy was used in a manner similar to that used by Ernst and Hennig (1994) such that the FID was examined in the time-domain providing a sub-millisecond temporal resolution. In a previous study, Petridou, Plenz et al. (2006) analyzed the frequency-domain of the FID in spontaneously active organotypic rat brain cultures. They showed a phase difference, and a lesser magnitude difference, at the frequencies of electroencephalographic recordings obtained outside of the MRI. In contrast, the present study measured the FIDs following evoked nerve cord simulation in a time-locked fashion and examined the differences of the time-domain signal between the presence and absence of an action potential. In addition to this experiment, a volume conductor model was adapted to calculate the FID magnitude and phase change from a previously reported intracellular recording of an earthworm action potential (Kao and Grundfest 1957). The MRS experiment showed a phase change that was in agreement with the theoretical predictions of the volume conductor model.

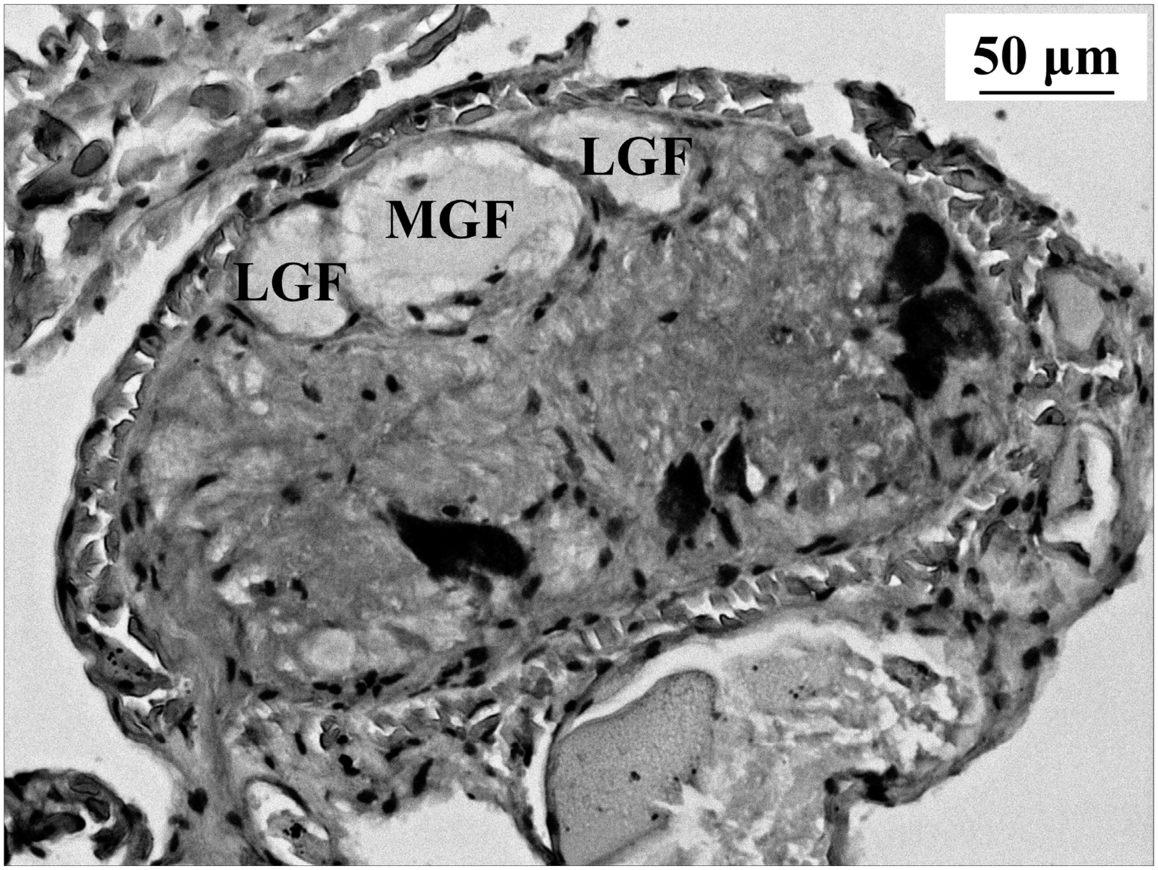

Figure 2-1 Earthworm Nerve Cord Cross-Section: A section through the isolated earthworm nerve cord. The median giant fiber (MGF) separates the two electrically coupled lateral giant fibers (LGF). 9-µm paraffin section stained with hematoxylin.

2-3 Materials and Methods

2-3.1 Earthworm Nerve Cord Preparation. Earthworms (*Lumbricus terrestris*, Kennesaw Bait Co., Marietta, GA) were anesthetized in 10% ethanol for 5 min, or until the escape reflex was abolished, and submerged in a 0°C dissection chamber containing worm saline (77.0 mM Na^+, 4.0 mM K^+, 6.0 mM Ca^{2+}, 1.0 mM Mg^{2+}, 43.0 mM Cl^-, 26.0 mM SO_4^{2-}, 2.0 mM Tris, 55.0 mM sucrose, 167.0 mOsm and 7.4 pH) (Drewes and Pax 1974). A longitudinal incision was made along the dorsal midline to access the ventral nerve cord. The nerve cord was then isolated from the worm by gently peeling the cord from the ventral epithelial wall and cutting any connective tissue. The worm saline was changed every 15 min for the duration of the dissection. Once the nerve cord was removed, it was transferred to 4°C saline and allowed to acclimate to room temperature before being transferred to the chamber for simultaneous field potential recordings and MRS.

2-3.2 Chamber Allowing Simultaneous Field Potential Recordings and MRS. The chamber to record simultaneous field potentials and MRS was constructed with two compartments linked by a glass capillary bridge (inner diameter = 0.7 mm, outer diameter = 1.0 mm) and was filled with worm saline (Fig. 2-2). The first compartment contained a pair of bipolar AgCl hook stimulating electrodes (1 mm separation) and the entrance AgCl hook recording electrode (located directly before the entrance of the capillary bridge). The second compartment contained the exit AgCl hook recording electrode (located directly after the exit of the capillary bridge) and the common reference AgCl electrode. A custom radio-frequency (RF) transmit and receive microcoil (inner diameter = 1 mm, number of turns = 7, copper wire diameter = 0.405 mm, coil length = 4 mm, enamel insulation thickness = 20 μm) was wound tightly around the glass capillary bridge and fixed with cyanoacrylate (Minard and Wind 2001, Part I; Minard and Wind 2001, Part II). The RF microcoil recorded the FID.

The anterior end of the nerve cord was pinned over both stimulating electrodes and gently drawn through the capillary bridge and through the center of the RF microcoil by applying slight suction. The nerve cord fit tightly within the inner walls of the capillary bridge and was turned until the MGF was located at the bottom edge of the capillary's inner diameter. In this way, the MGF was asymmetrically positioned at the bottom extreme of the microcoil's sensitive volume since the MGF is located on the dorsal surface of the nerve cord (Fig. 2-1). The posterior end of the cord was secured over the exit electrode and the remaining nerve cord was gently stretched and secured over the entrance electrode. All fastening pins were non-magnetic cactus spikes.

2-3.3 Data Acquisition – Electrophysiology. Action potentials were recorded by a Digidata 1320A (Axon Instruments, Sunnyvale, CA) in response to nerve cord stimulation by a pulse generator (Master-8, A.M.P.I., Jerusalem, Israel). A stimulus pulse with a 1.0 ms delay and 0.3 ms width was used (Fig. 2-3). The amplitude of the pulse was controlled by a stimulus isolator (A360 stimulus isolator, World Precision Instruments, Sarasota, FL). The threshold stimulation for action potential generation was determined before each trial by adjusting the stimulus magnitude to elicit action potentials about half the time.

The stimulus amplitude was kept constant within a single trial but was reset to the action potential threshold between trials, if necessary. The two recording and one reference electrode measured the extracellular field potential differentially (Differential AC Amplifier, Model 1700, A-M Systems, Sequim, WA). The following parameters were used: 500 repetitions per trial, 10 kHz sampling bandwidth, 2.05 s sampling duration, 4 s inter-stimulus interval, 1 kHz low-pass filter and 300 Hz high-pass filter. Clampex 9.2 (Axon Instruments) stored the amplified, filtered and digitized electrophysiological time courses.

2-3.4 Data Acquisition – MRS. The chamber was placed at the isocenter of a 9.4 T Bruker Biospin (Billerica, MA) with the nerve cord arranged perpendicular to the static magnetic field. The following parameters were used: 3.125 kHz FID sampling bandwidth, 90^o flip angle, 2.0 s repetition time (T_R), 1,000 repetitions per trial and 6 dummy scans. Each experiment lasted 7-10 hr. The transmit and receive microcoil used quadrature detection to simultaneously acquire the real and imaginary components of the FID. During even T_R's, the MRS protocol was initiated without triggering the nerve cord stimulation. This group was used in post-processing steps to correct for phase drift. During odd T_R's, the nerve cord was stimulated at the threshold of action potential generation. Two interleaved subgroups resulted during the odd T_R's due to the all-or-nothing nature of the action potential – action potential (AP) and no action potential (nAP) subgroups.

A RF excitation delay was determined at the start of each trial according to the trial-specific conduction velocity calculated by linearly extrapolating the difference in arrival times of the action potential at the two recording electrodes.

This delay was calculated in order to fix the arrival of the action potential at 0.5 ms after the start of FID acquisition (Fig. 2-3). No magnetic field gradients were used during the experiment. Within a single experiment, if action potentials could no longer be elicited from the nerve cord, then further trials were discontinued. If the nerve cord was healthy for at least seven full trials (with a maximum of 12 trials), then the worm was considered for further data analysis.

2-3.5 Data Analysis – Electrophysiology. Field potentials were acquired from both recording electrodes for every T_R. Using Clampfit 9.2 (Axon Instruments), each repetition was separated into the components that corresponded to the even and odd T_R's, respectively. The absences of stimulation artifact and nerve cord activity were verified in the even T_R group and were not used for further analysis. The presence or absence of an action potential event was then identified for each odd T_R trace using a Clampfit 9.2 threshold detection program and separated into AP and nAP subgroups, respectively. Finally, the baseline for each trace was corrected to zero.

2-3.6 Data Analysis – MRS. The interleaved MRS time courses were separated into odd and even T_R groups. The phase information was processed by multiplying individual odd T_R FIDs by the complex conjugate of the subsequent even T_R FID. The MRS time courses were then separated into AP and nAP subgroups according to the electrophysiological recordings that were simultaneously acquired. The phase of the FID was calculated and filtered (8-pole Bessel band-pass filter, Clampfit 9.2, Axon Instruments) to remove frequencies outside of the 240 - 437.5 Hz range. This range included physiological frequencies of the action potential and minimized filtering artifacts.

2-3.7 Correction of Action Potential Timing Based on Conduction Velocity. A single action potential reference trace was chosen for each worm and individual action potential electrophysiology traces were shifted in time around it. A “shift value” was accepted when a maximum positive Pearson’s linear correlation coefficient was achieved between the two traces. The shift value is the amount of time an individual action potential trace required to achieve maximal alignment with the reference trace. This correction was performed only on exit electrode time courses and the shift values were then used to shift the corresponding FID and entrance electrode time courses. Events that had a correlation coefficient three standard deviations below that of the mean correlation coefficient of a single worm were rejected from further analysis. Once the action potentials were temporally aligned, the mean action potential minimum was used to normalize the electrophysiolgical data.

The nAP subgroup FIDs were also shifted to control for the effects of the action potential alignment process. This was done by assigning shift values to individual nAP FIDs that were randomly sampled from the accepted AP subgroup shift values. Shift values from the AP and nAP subgroups were then compared with a t-test to verify that they were from the same population with at least 95% confidence. The process of shifting the nAP FIDs was repeated 100 times and averaged to ensure reproducibility of the nAP waveform presented in Fig. 2-4C.

2-3.8 Modeled Magnetic Resonance Magnitude and Phase Change. The theoretical model of Woosley, Roth et al. (1985) was used to calculate the magnetic field of the earthworm MGF using a previously reported earthworm intracellular potential recording (Kao and Grundfest 1957).

$$B(\rho, k) = i\mu_0 a k I_1(|k|a) K_1(|k|\rho) \left\{ \frac{\sigma_i}{\beta(|k|a)} - \frac{\sigma_e}{\alpha(|k|a)} \right\} \phi_m(k) \qquad \textbf{Eq.2-1}$$

Where ρ is the radial distance from the axon center, k is the spatial frequency, B is the spatial Fourier transform of the magnetic field at distance ρ, $i = \sqrt{-1}$, μ_0 is the permeability of free space, a is the axon radius, I_1 and K_1 are modified Bessel functions, α and β are defined by the Bessel functions, σ_i and σ_e are the intracellular and extracellular conductivities, respectively, and $\phi_m(k)$ is the spatial Fourier transform of the intracellular potential (Woosley, Roth et al. 1985). The MGF occupies the dorsal surface of the nerve cord (Fig. 2-1) and was turned in the experiment and theoretical simulation to occupy the extreme bottom position of the microcoil's sensitive volume. The component of the generated magnetic field that integrates with B_0 (z-component) was calculated at varying distances within the volume of the solenoid microcoil. The following values were used to calculate the magnetic field of a single action potential: ρ = 36-4,000 µm, a = 35 µm, u = 14.7 m/s, σ_i = 1.70 S/m and σ_e = 2.06 S/m.

The magnitude and phase changes associated with the calculated z-component of the axonal magnetic field were determined:

$$\phi(r, \theta, l, t) = \gamma \int B(r, \theta, l, t)\, dt \qquad \textbf{Eq. 2-2}$$

$$Me^{i\Delta\phi(t)} = \frac{M_o}{V} \iiint r \cdot e^{i\phi(r, \theta, l, t)}\, dr\, d\theta\, dl \qquad \textbf{Eq. 2-3}$$

The resultant phase (ϕ) was determined for each time point (t) of the calculated magnetic field over the sensitive volume of the solenoid RF microcoil (V), where r is the glass capillary inner diameter, θ is the radial angle, l is the length of the microcoil and γ is the proton gyromagnetic ratio. Finally, the MR magnitude (M) and phase change ($\Delta\phi$) were calculated in time, where M_o is the equilibrium magnetization.

Kao and Grundfest's (1957) description of spike rise time, peak potential amplitude and time of spike decay to baseline were considered in reconstructing the intracellular recording and was used in our theoretical simulation. The MGF radius was experimentally measured. Isolated nerve cords were fixed in 4% paraformaldehyde for 60 min, cut into coronal sections and embedded in paraffin. Blocks were cut at 9 µm, deparaffinized and stained with hematoxylin (GeneTex, Inc GTX73341). The radius of the MGF in the posterior nerve cord was calculated from its circumference using an Axio Scope Observer.A1 and AxioVision 4.7 (Carl Zeiss MicroImaging GmbH, Jena, Germany).

A Pearson's linear correlation was performed between the theoretical and experimental phase time courses. In order for a point-by-point analysis to be performed, several adjustments were made. First, the sampling interval of the theoretical simulation was adjusted to that of the experimental interval (0.32

ms). The theoretical phase minimum value was preserved during this process and the phase change was set to begin at approximately 0.5 ms. The latter adjustment synchronized the arrival of the theoretical action potential with the experimental action potential, which was calculated to arrive 0.5 ms after the start of FID acquisition.

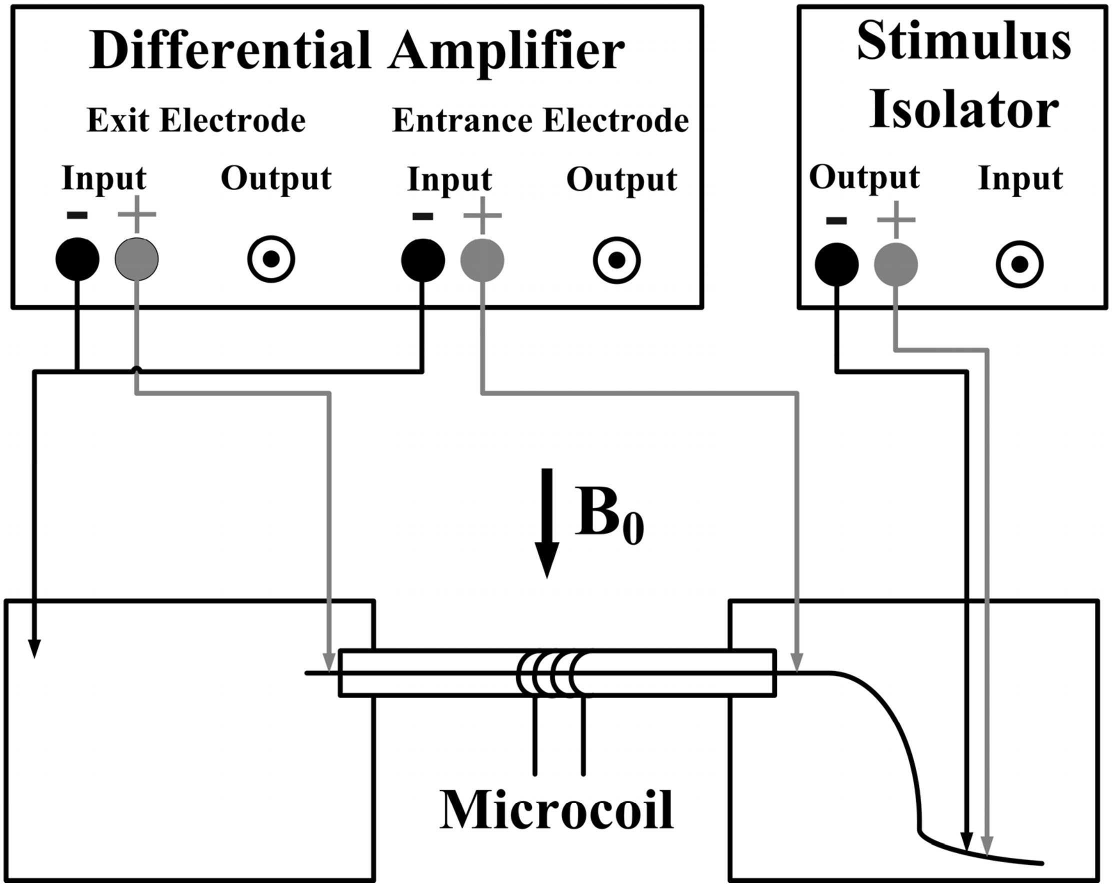

Figure 2-2 Chamber Allowing Simultaneous Field Potential Recordings and MRS: The anterior nerve cord was stimulated with bipolar electrodes at the threshold of action potential generation. This resulted in interleaved events with action potentials and without. Evoked action potentials were first recorded by the entrance electrode and followed by the exit electrode. The difference in arrival time of the action potential between the two electrodes was used to calculate the conduction velocity. The conduction velocity then was used to determine the time at which the action potential arrived at the custom RF microcoil.

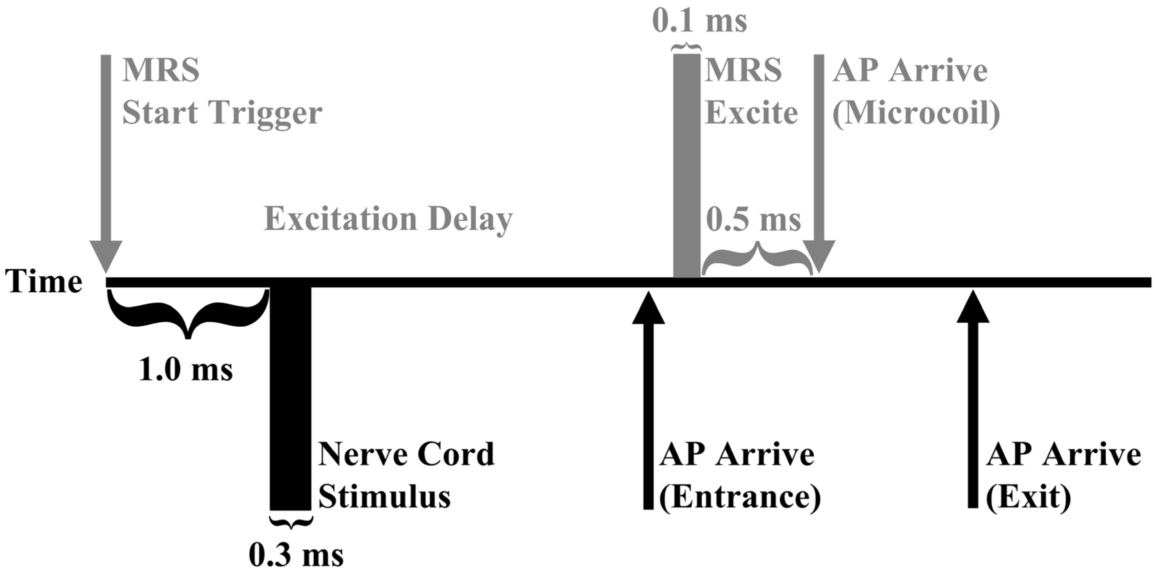

Fig. 2-3 MRS Timing Diagram: Timing diagram of the simultaneous field potential recordings (black text) and MRS (gray text) experiment. A trigger from the MRS protocol initiated the field recording digitizer and the nerve cord stimulus pulse generator (1.0 ms delay, 0.3 ms width). A trial specific excitation delay was calculated according to the predetermined conduction velocity of the action potential (AP) between the entrance and exit field recording electrodes. The MRS excitation (0.1 ms width) was timed so that the action potential arrived at the RF microcoil 0.5 ms after the start of FID acquisition.

2-4 Results

2-4.1 Measuring an Evoked Action Potential with Simultaneous Electrophysiology and MRS. The nerve cords of 6 earthworms (59 trials) with a weight of 4.90 ± 0.05 g (*M* ± *SEM*) before dissection and an average conduction velocity (u) at room temperature of 14.7 ± 0.1 m/s were used. A total of 29,638 electrophysiological traces were obtained, with 16,718 (56%) having an action potential (AP subgroup) and 12,920 (44%) exhibiting no action potential (nAP subgroup).

The field recordings measured activity from the entire nerve cord at the location of the electrode. Stimulus intensity was adjusted to evoke a single action potential at the entrance and exit electrodes (Figs. 2-4A and 2-4B, respectively). The absence of other extracellular potentials verified the successful isolation of the MGF action potential from all other cellular components. The temporal evolution of the action potential was consistent throughout the course of each experiment, suggesting that the preparation was stable over the course of a 7-10 hr experiment.

No change could be identified in either the magnitude or the phase of a single FID trace. However, the mean AP and nAP FID traces of all 6 worms (Fig. 2-4C) revealed a difference in the phase, but not in the magnitude, that was associated in time with the action potential. The peak trough had a group averaged difference in phase (AP – nAP) of [-1.1 ± 0.3] x10^{-5} at 1.28 ms and [-1.2 ± 0.3] x10^{-5} radians at 1.60 ms, respectively.

2-4.2 Theoretical MR Magnitude and Phase Change. Two isolated nerve cords, from earthworms weighing 4.55 and 5.09 g before dissection, were used to measure the MGF radius. The MGF radius of the posterior nerve cord was 35.1 ± 0.8 µm, calculated from the circumference of 45 nerve cord sections. Simulation of an earthworm action potential indicated a maximum magnitude change of -2.39 x 10^{-9} % (Fig. 2-5A) and phase change of -0.69 x 10^{-5} radians (Fig. 2-5B) in the FID. The predicted magnitude change was below the detection threshold for our MRS method by at least 10,000 times. The measured and simulated phase changes, on the other hand, were of similar magnitudes. The magnitude and phase returned to baseline at the completion of the action potential.

2-4.3 Correlation of Theory and Experiment. The mean of all nAP phase time courses (n = 12,920) was subtracted from the mean of all AP phase time courses (n = 16,718) to calculate the experimental phase change. A Pearson's linear correlation between the simulated and experimental phase change had a correlation coefficient (r_e) of 0.802 ($p < 0.001$, n = 17 time points) (Fig. 2-6).

2-2.4 Individual Worm Analysis. The mean nAP phase time course was subtracted from the mean AP phase time course for each individual earthworm. Figure 2-7 presents the mean phase for the earthworms following the subtraction (n = 6) over the 17 time points (0.00 – 5.12 ms). The data were analyzed using a repeated measures one-way ANOVA, $F(16,80) = 1.46$, p = 0.14. A post-hoc one sample t-test compared the mean phase for the 6 earthworms to zero for each of the 17 time points. These comparisons revealed that the two trough points had the following values: 1.28 ms, t (5) = -3.93, p = 0.011 and 1.60 ms, t (5) = -3.54, p = 0.017. The 15 other time points had p-values greater than 0.11.

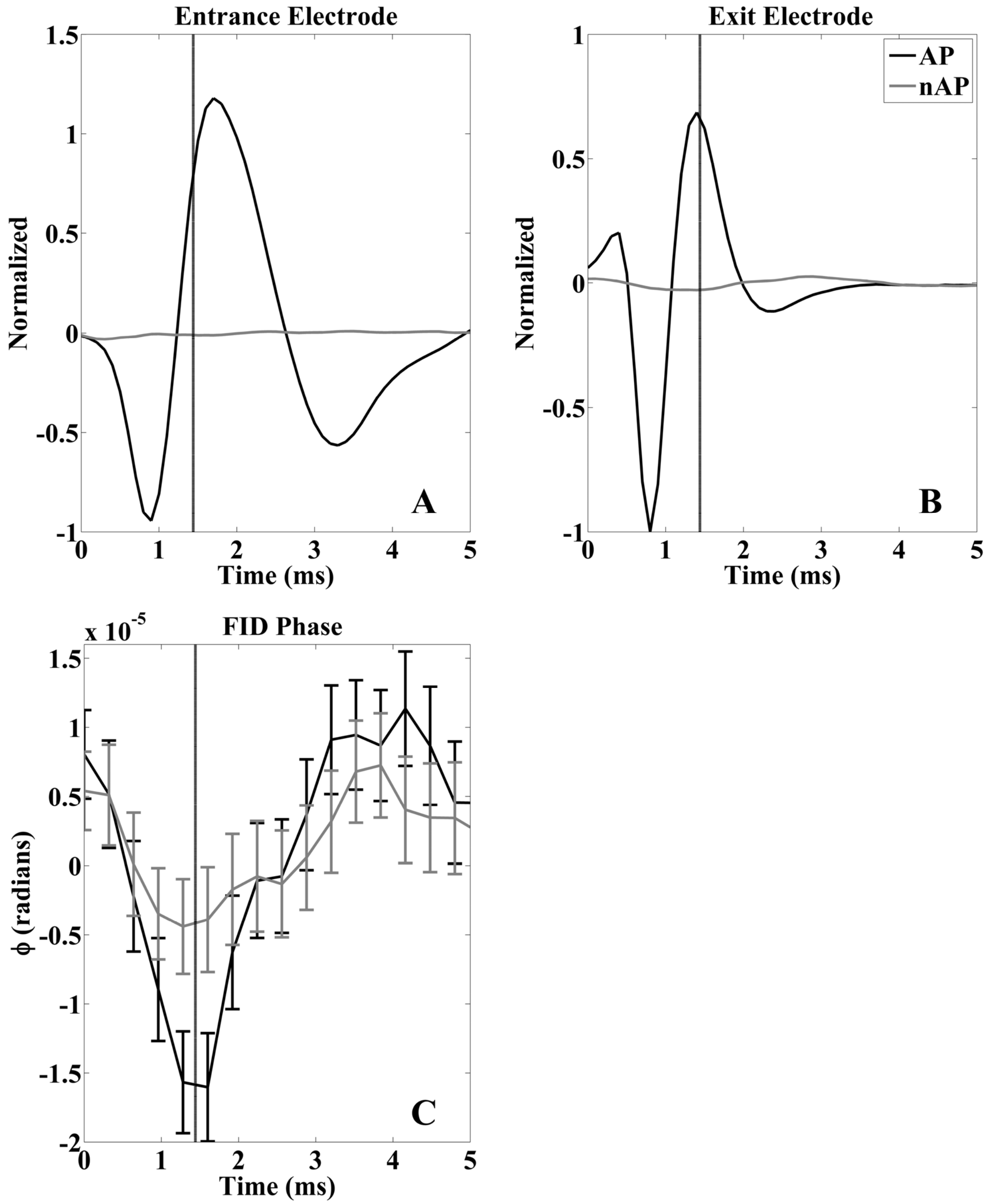

Figure 2-4 Experimental Field Potential Recordings and FIDs: The averaged time course of the action potential field at the entrance (A) and exit (B) of the capillary bridge and the averaged FID phase (C). Averaged time courses with the presence of an action potential (AP subgroup) are marked in a solid

black line while those identified as not having an action potential (nAP subgroup) are marked with a solid gray line. The action potential arrived at the RF microcoil 0.5 ms after the start of FID acquisition. The action potential conduction velocity was used to adjust the electrophysiological time courses in panels A and B to be consistent with the arrival of the action potential at the microcoil in panel C in order to synchronize all traces. In this way, the vertical lines represent the same relative cycle of the action potential that corresponds to the trough of the FID phase. Error bars represent the SEM and the number (n) of AP and nAP time courses are 16,718 and 12,920, respectively.

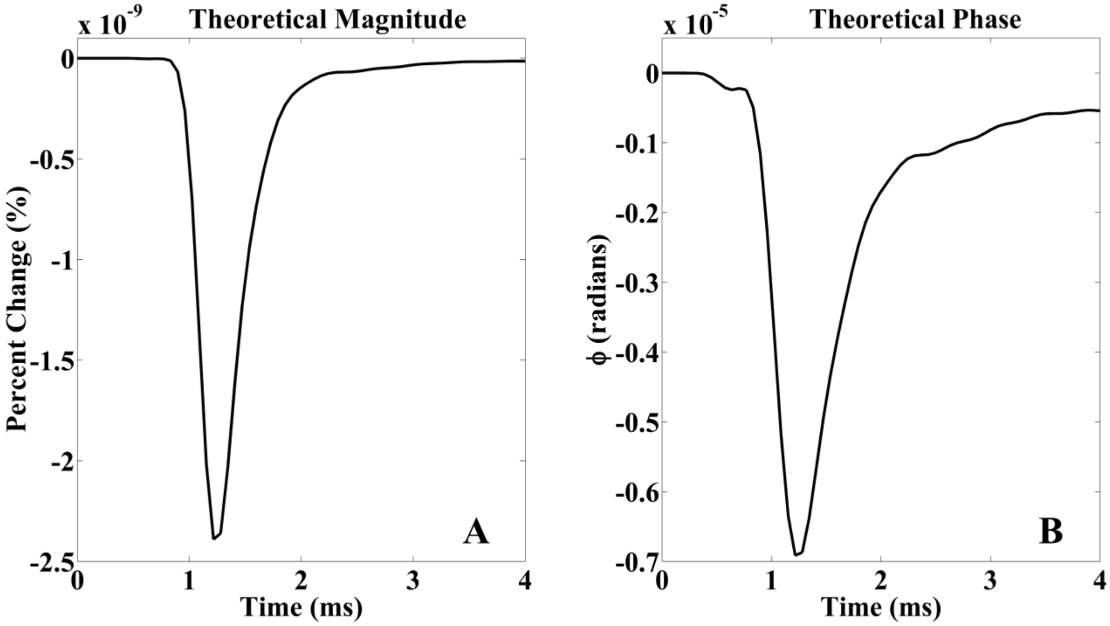

Figure 2-5 Theoretical Magnitude and Phase Changes in the FID: The MGF transmembrane potential of a single evoked action potential was described by Kao and Grundfest (1957) and used in our theoretical simulation. The theoretical MR magnitude (A) and phase (B) time courses were calculated for a single earthworm action potential. The following parameters were used in calculating the theoretical time courses: ρ = 36-4,000 µm, a = 35 µm, u = 14.7 m/s, σ_i = 1.70 S/m and σ_e = 2.06 S/m.

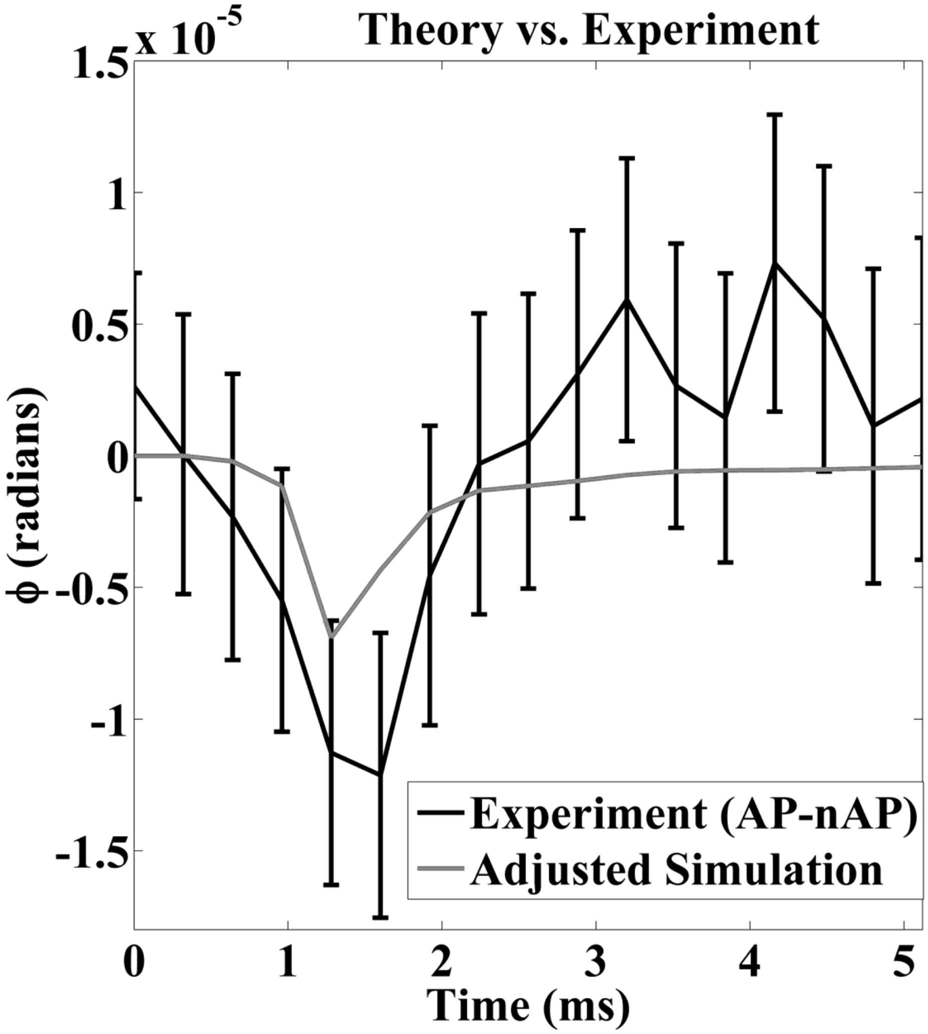

Figure 2-6 Comparing Theory and Experiment: All phase time courses from the six worms were separated into action potential (AP) (n = 16,718) and no action potential subgroups (nAP) (n = 12,920) and averaged. The average nAP phase time course was subtracted from the average AP (solid black line) and correlated with the simulated phase change (dashed gray line) (correlation coefficient (r_e) = 0.802, $p < 0.001$, n = 17 time points for each trace). The error bars represent the 95% confidence intervals for the subtraction. The adjusted simulation has the same sampling bandwidth and action potential arrival time as the experiment.

Repeated Measures 1-Way ANOVA

	SS ($x10^{-10}$)	df	MS ($x10^{-10}$)	F	P
Treatment (Time Points)	28.1	16	1.8	1.46	0.14
Individual (Earthworms)	6.2	5	1.2	1.03	0.41
Residual	96.4	80	1.2		
Total	130.7	101			

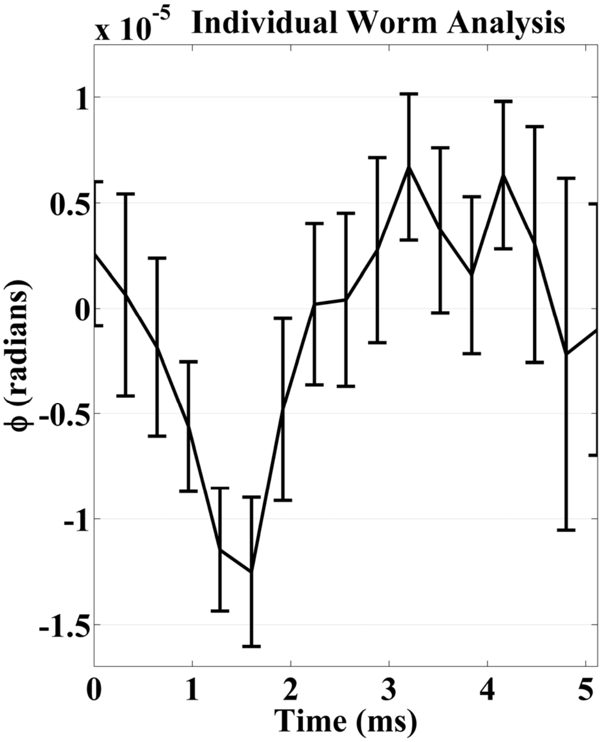

Post-Hoc One Sample T-Test

Time (ms)	T	P
0.00	0.7561	0.4837
0.32	0.1342	0.8985
0.64	-0.4393	0.6788
0.96	-1.8221	0.1281
1.28	-3.9340	0.0110
1.60	-3.5449	0.0165
1.92	-1.1101	0.3175
2.24	0.0535	0.9594
2.56	0.1002	0.9241
2.88	0.6271	0.5581
3.20	1.9304	0.1114
3.52	0.9482	0.3866
3.84	0.4218	0.6907
4.16	1.8025	0.1313
4.48	0.5417	0.6113
4.80	-0.2620	0.8038
5.12	-0.1691	0.8724

Figure 2-7 Statistical Analysis of Individual Worm Subtractions: The average nAP subgroup was subtracted from the average AP subgroup for each of the 6 earthworms (n = 6) over the 17 time points (0.00 – 5.12 ms). The 6 phase time courses that resulted from the subtraction were analyzed by a repeated measures 1-way ANOVA (SS = sum of squares, df = degrees of freedom, MS = mean squares, F = f-statistic, P = p-value). The mean of the 6 time courses was plotted (*M* ± *SEM*) and a one sample t-test was performed on each time point (T = t-statistic, P = p-value, df = 5).

2-5 Discussion

Our results demonstrate the feasibility of detecting an evoked axonal action potential in the absence of the hemodynamic response. MRS detected a significant phase change, but not a magnitude change, in the FID that corresponded in time with simultaneous electrophysiological recordings of the action potential. The amplitude of the FID averaged phase change was similar to the theoretical phase change determined using a volume conductor model. These experiments provide definitive evidence for the direct detection of an NMF by MRS that agree with the theoretical prediction in both temporal profile and amplitude.

2-5.1 Technical Considerations. There were small variations in conduction velocity within a single trial that resulted in action potentials arriving at the entrance and exit electrodes at slightly different times. The misalignment of action potentials resulted in a blurred group average field potential. This action potential misalignment would have also occurred at the microcoil and would cause a temporal blurring of the average FID. Electrophysiological data from the exit electrode were used to correct for this misalignment by registering each action potential to a reference trace. The single electrode registration was then used to correct for the timing misalignment at the entrance electrode as well as the FID signal. This correction assumed that the conduction velocity was constant between the entrance and exit electrodes. Although there is some evidence of variation in the conduction velocity along the length of the earthworm nerve cord (McFall, Landa et al. 1977; O'Gara, Vining et al. 1982), action potentials having a fast conduction velocity (1.4 cm/ms) allow for an acceptable approximation over the short distances between the entrance and exit electrode (2.7 cm) and the microcoil center and exit electrode (1.4 cm).

A slow variation was seen in the nAP subgroup average (Fig. 2-4C). This was most likely due to the current injection applied to stimulate the nerve cord. This effect was controlled for in the present study by keeping the experimental conditions identical for AP and nAP subgroups and examining the difference (Fig. 2-6 & 2-7).

We reported a theoretical (Fig. 2-5B) and an adjusted phase simulation (Fig. 2-6). The adjusted simulation included adjustments based on sampling interval and the action potential arrival time of the experiment. It was possible to compare the simulation directly to the experimental results following these adjustments. The time course of the adjusted simulation significantly correlated to the experimental phase changes in both temporal characteristics and peak minima. Yet, the experimental phase peak appeared wider in time than the simulation. This difference might be attributed to less accurate correction of the action potential misalignment as the distance increased from the exit electrode.

The effect of the MGF radius on the depth of the theoretical phase minimum was also examined. It is known that the processes of fixing and embedding will cause tissue shrinkage (Ross 1953; Hillman 2000). Although the degree of shrinkage for this specific tissue is not known, the radius of the MGF was reported to be between 34 and 47 μm with the radius decreasing from anterior to posterior (McFall, Landa et al. 1977). An approximately linear relationship between the predicted phase minimum and the MGF radius was observed across this range. For every 2 μm increase in the radius, the phase minimum deepened by -0.09 $x10^{-5}$ radians.

Lastly, we did not consider the magnetic field that existed inside the MGF in the theoretical modeling. Previous studies did not validate this component of the magnetic field with experimental results and it was omitted to achieve a more conservative model. The magnetic field inside the MGF would cause only a slightly larger simulated FID phase change as the omitted volume accounts for only 1% of the total volume seen by the microcoil.

2-5.2 Phase Difference. The FID phase difference was examined by pooling AP and nAP phase time courses in two ways. The first method grouped all AP (n = 16,718) and nAP (n = 12,920) time courses from the six earthworm experiments and subtracted their means (Fig. 2-6). This pooling method had the advantage of a large sample size, but did not uniformly represent each earthworm due to our method of action potential generation. Nerve cord stimulation was set at the threshold of action potential generation, which created the AP and nAP subgroups from a single stimulation intensity. In this way, the exact number of generated action potentials could not be controlled and individual worms had different ratios of action potentials to no action potentials. In addition, the number of trials depended on the nerve cord and varied from 7 to 12 (500 time courses per trial). Earthworms with a greater number of trials were, therefore, overrepresented by pooling all time courses.

The second pooling method averaged the AP and nAP subgroups for each individual earthworm before subtraction. Therefore, there was one subtracted time course for each of the 6 earthworms. Fig. 2-7 presents the average of these 6 time courses. This pooling method created an equal representation of each earthworm experiment and better controlled for inter-experimental variation. The one-way ANOVA indicated that no time point was statistically different from the other 17 time points. The one sample t-test with an α-value (0.05) adjusted for 17 multiple comparisons agrees with the conclusions drawn from the ANOVA ($\alpha = 0.05/17 = 0.003$). However, the two time points at the trough of the FID phase have notable p-values of 0.011 at 1.28 ms and 0.017 at 1.60 ms (Fig. 2-7).

2-5.3 Volume Conductor Model. Roth and Wikswo (1985) compared an experimentally recorded axon magnetic field to one that was predicted by the volume conductor model (Woosley, Roth et al. 1985). Their measured magnetic field showed significant consistency with the predicted in both the magnetic field magnitude and temporal evolution. In addition, the toroid detector from which Roth and Wikswo's recorded the axon magnetic field was similar to the RF microcoil detector in our experiment. Both types of detectors average the magnetic field over the circumference and length of the detector. For these reasons, we had confidence that an adaptation of the volume conductor model would correctly predict the MR magnitude and phase change following an evoked action potential using our methods.

The volume conductor model predicts the total axon magnetic field from the individual contributions of the extracellular and intracellular currents, I_e and I_i, respectively. It was previously determined that the magnetic field due to I_e was orders of magnitude less than the magnetic field due to I_i (Woosley, Roth et al.

1985). In this way, a good approximation of the total axon magnetic field can be calculated by considering only the contribution of I_i. The intracellular current conducting longitudinally through a defined axonal compartment can be characterized as an equivalent current dipole (Q_i) and is a relevant measure of brain activity that is often used in the discussion of magnetoencephalographic and electroencephalographic measurements. The equivalent current dipole is a vector quantity described by the equation $Q_i = I_i L dr$ (Murakami and Okada 2006; Cassarà, Hagberg et al. 2008), where L is the MGF length within the microcoil (4 mm) and dr is a unit direction vector (dr = 1 for the MGF being perpendicular to B_o). The volume conductor model was extended to calculate I_i in time for our simulated action potential and Q_i was estimated to have a maximum change of -1.0 nAm in time.

2-5.4 Symmetrical vs. Asymmetrical Distribution of the NMF. Chow, Cook et al. (2006) examined the phase changes that resulted from a symmetrically and asymmetrically distributed NMF within a volume of interest. They determined that the magnetic field must be asymmetrically distributed in the volume for a phase change to be detected, since a net zero phase change resulted from a symmetrically distributed magnetic field. A solenoid microcoil with an asymmetrically positioned axon was used in our experiment and theoretical simulation. The earthworm nerve cord in our experiment was tightly contained within the inner walls of the capillary bridge and the MGF was located at the bottom edge of the capillary's inner diameter. An adaptation of the volume conductor model predicted the z-component of the magnetic field generated by the MGF from this position within the microcoil. In this way, the MGF bipolar magnetic field was asymmetrically distributed in the volume of interest and resulted in a detectable phase change.

A circular surface microcoil positioned above the capillary bridge and perpendicular to the MGF is an alternative method in investigating the phase change associated with the axon NMF. A coil of this design has diminishing sensitivity to the proton signal as the distance from the surface coil increases and permits an asymmetric sensitivity to the phase change caused by the axon NMF. In this way, a surface microcoil design may enhance the detectability of the phase change, since it is more sensitive to a single pole of the NMF, in contrast to our solenoid design that is equally sensitive to both poles. However, a surface microcoil will lose sensitivity as the distance from the MGF increases, whereas the axon drawn through a solenoid microcoil will not.

2-5.5 Physiology of the Phase Change. The shape of the FID phase difference in both the predicted and measured time courses is due to the opposing sodium and potassium currents that occur during an action potential. The action potential begins with the depolarizing stimulus at the anterior end of the MGF. Depolarization opens fast acting voltage-gated sodium channels and allows an inward flux of sodium ions into the axon. This inward current creates a magnetic field that temporarily opposes the external magnetic field resulting in a decrease in the net magnetic field and a drop in the FID phase. The voltage-gated sodium channels quickly inactivate and prevent the flux of new sodium ions from entering the axon. At a similar time that the sodium channels inactivate, slower activating voltage-gated potassium channels open and allow potassium ions to leave the axon. This opposing outward current reverses the magnetic field generated by the axon and subsequently increases the net magnetic field and returns the FID phase to baseline. This temporal evolution on a sub-millisecond scale requires an MR method that has sufficient temporal resolution as is demonstrated by our experiment.

The simulated phase change in Fig. 2-6 shows two means at the times 3.20 and 4.16 ms to be outside of the experimental phase change confidence intervals. These time points are above zero radians, which suggest that the refocusing magnetic field generated by the axon was stronger than the theoretically predicted magnetic field. A stronger refocusing magnetic field may be due to a greater outward potassium current that corresponds to a hyperpolarization of the axon in the final stages of the action potential. The intracellular recording of Kao and Grundfest (1957), used in our theoretical simulation, did not have an axon hyperpolarization component and may be due to differences in the physiological saline solutions of each experiment. The extracellular saline solution of our experiment was consistent with the ionic composition measured in the coelomic fluid of the earthworm (Drewes and Pax 1974), while that of Kao and Grundfest was not. This difference could result in a change in the inward and outward current characteristics of each experiment. However, the intracellular recording of Kao and Grundfest is an appropriate approximation because the phase change associated with the hyperpolarizing component of the action potential will contribute very little to the total magnetic field change. This is evident in our observations as other simulated phase points between 2.88 and 5.12 ms are within the 95% confidence intervals of the experimental phase change.

2-5.6 Lorentz Effect Imaging. Lorentz effect imaging (LEI) and its application to the direct detection of magnetic fields was shown in current carrying phantoms (Song and Takahashi 2001; Truong, Wilbur et al. 2006) and *in vivo* (Truong and Song 2006). The Lorentz force is the spatial displacement of a current carrying conductor in the presence of an external magnetic field that is equal to the cross product of the current vector and the magnetic field. MR contrast arises from the Lorentz force by the spatially incoherent displacement of water protons caused by the conductor's compression of the surrounding elastic medium or by the bulk movement of water by ionic current flux (Truong, Avram et al. 2008). LEI enhances this displacement with oscillating magnetic field gradients to cause a loss of phase coherence, which causes a decrease in the MR signal magnitude. The Lorentz effect occurs at a time simultaneous to the electrical activity and can confound our study.

However, it is believe that the Lorentz force has a minimal effect on the FID phase in the MRS technique used herein, since previous LEI shows no magnitude change during excitation of the human median nerve without the use of strong oscillating magnetic field gradients (Truong and Song 2006). Applied magnetic field gradients, including spatial encoding gradients, were absent in our experiment. In addition, the close correlation of the simulated to the observed FID phase change provides further evidence that the Lorentz forces may contribute a phase change that is significantly less than the change associated with the axon NMF. Estimates of water displacement caused by both the spatial displacement of the axon and the ionic current flux are necessary in order to predict the changes to the FID signal caused by the Lorentz force.

Extrapolation to *In Vivo* Studies and Application. Previous studies have measured a magnitude, but not a phase, change in the MRI signal following visual stimulation of the human optic nerve at 1.5 T (Chow, Cook et al. 2006; Chow, Cook et al. 2006). However, a similar study failed to replicate these findings at 3 T and attributed this failure to increased magnetic susceptibility artifacts at the higher field (Chow, Dagens et al. 2008). We have demonstrated through experiment and simulation that the phase of the MR signal is more sensitive to evoked axonal magnetic fields and that the effect of the axonal magnetic fields on the MR signal takes place on a millisecond timescale. The latter aspect would call for MR studies with a high temporal resolution, as demonstrated here. For *in vivo* studies along this line, spectroscopic imaging with the examination of the time-domain data may be used.

The volume conductor model can predict the intracellular membrane potential from the measured magnetic field (Roth and Wikswo 1985; Woosley, Roth et al. 1985). In combination with our method to detect NMFs, *in vivo* axon function can be measured following activation. Such non-invasive study of neural currents localized to specific nerve fiber bundles could be developed further to establish characteristics of action potential propagation in normal and disease states, such as multiple sclerosis. However, MR signal changes attributable to the hemodynamic response to the nerve activation, which was absent in our experiment, would need to be addressed for application to *in vivo* study.

2-6 Conclusion

We demonstrated the direct detection of a single evoked axon magnetic field in the earthworm using simultaneous MRS and electrophysiology in the absence of the hemodynamic response. This experiment was validated by comparing the measured FID phase change with an adaptation of Woosley, Roth et al.'s volume conductor model (1985). We also showed that the phase of the FID returned to baseline at the cessation of the axonal event and that a method with a high temporal resolution is required to resolve such transient neural magnetic fields, therefore validating MRS as an alternative method for the direct detection of neural activity.

CHAPTER 3

Examining the Direct Detection of Evoked Potentials in the CA1 Region of the Rat Hippocampus with Magnetic Resonance Spectroscopy

3-1 Abstract

Functional magnetic resonance imaging (fMRI) is a technique used to study *in vivo* brain activation by indirectly measuring signal changes that originate from the hemodynamic response. In this way, the fMRI signal is spatially and temporally inaccurate to the electrical signals of the brain. Direct detection of neural magnetic fields (NMFs) by magnetic resonance (MR) technology can accurately measure electrical activity of the brain, but its application to measuring neural responses of the human brain is contaminated by the hemodynamic response. The current study combines simultaneous field potential recordings and magnetic resonance spectroscopy (MRS) to assess the feasibility of detecting evoked NMFs from the CA1 region of the rat hippocampal slice following stimulation of the Schaffer collaterals. Measurement of the free-induction decay (FID) phase and magnitude changes were compared to the theoretically predicted MR signal changes induced by the evoked activity of a similar CA1 volume (Cassarà, Hagberg et al. 2008). Activity of the hippocampal slice was terminated in the control condition and the detection threshold of the FID phase was determined to be 25-100 times greater than the predicted phase changes. These data suggest that the direct detection of evoked hippocampal NMFs is not possible under the current experimental methods and that the measurement of NMFs originating from gray matter is not currently practical.

3-2 Introduction

fMRI is a technique used to study *in vivo* brain function that indirectly measures the hemodynamic response to neural activation. The hemodynamic response is a complex interaction of changes in cerebral blood flow, cerebral blood volume and the cerebral metabolic rate of oxygen that supplies nutrients and removes waste of working neural tissue. The ratio of blood deoxyhemoglobin to oxyhemoglobin is the endogenous contrast agent that allows measurement of changes in the hemodynamic response. In this way, fMRI is an indirect measure of brain function since the MR signal change is located to the blood supply and is temporally inaccurate to the electrical signals of neural activity (Jezzard, Matthews et al. 2001).

The direct detection of NMFs would improve the spatial and temporal accuracy of brain functional imaging with MR technology. Early experiments directly detected magnetic fields in current carrying wires encased in water phantoms (Bodurka, Jesmanowicz et al. 1999; Konn, Gowland et al. 2003; Pell, Abbott et al. 2006). The magnetic fields generated by the wires were perfectly aligned with the static magnetic field (B_o) and achieved a maximum MR signal change. Computer simulations of NMFs improved these one-dimensional phantom studies by considering the three-dimensional arborized structures of the dendrites and axons (Xue, Gao et al. 2006; Park and Lee 2007; Cassarà, Hagberg et al. 2008). These computer simulation studies predicted MR signal changes that were below the signal changes contributed by the hemodynamic response. *In vivo* studies of evoked activity in the human brain reported findings that both supported (Xiong, Fox et al. 2003; Bianciardi, Di Russo et al. 2004) and opposed (Chu, de Zwart et al. 2004; Konn, Leach et al. 2004; Parkes, de Lange et al. 2007) the direct detection of NMFs with MRI. The hemodynamic response is present in these *in vivo* studies and contributes MRI signal changes that can confound NMF signal changes. Therefore, recent *in vitro* studies focused on physically decoupling the vasculature from the neural tissue. Spontaneous NMF activity was successfully detected in the dissociated rat brain culture (Petridou, Plenz et al. 2006), while a second study detected no MR signal change following evoked activity in the bloodless turtle brain (Luo, Lu et al. 2009). The synchronous nature of spontaneous activity contributes a larger and more detectable NMF compared to evoked activity and could account for the discrepancy between the studies.

Luo, Liu et al. (2009) examined the NMF in the *in vitro* intact bloodless turtle brain with attached eyes and used visual stimulation to evoked local field potentials (LFPs) in the turtle visual cortex. LFP and MRI data were acquired in an interleaved fashion to avoid electrophysiological artifacts produced by the MRI spatial-encoding magnetic field gradients. The turtle brain was submerged in artificial cerebral spinal fluid (ACSF) and aerated with O_2 gas. In a earlier study by the same group, Luo, Liu et al. (2007) determined that the dissolved O_2 gas in the ACSF contributed a 0.1% and 0.1^o change in the MR magnitude and phase, respectively. Therefore, a 0.1% magnitude change and a 0.1^o phase change were set as the detection threshold for the bloodless turtle brain experiment. No significant MR signal changes were recorded, which suggests that the signal change contributed by the NMFs was below these pre-defined detection thresholds . Theoretical simulation determined the signal change was far below these detection thresholds for evoked neural tissue and estimated a maximum MR magnitude change of -3 x 10^{-5}% and phase change of 0.001° (Cassarà, Hagberg et al. 2008).

Cassarà, Hagberg et al. (2008) predicted the magnetic field generated by a population of CA1 pyramidal neurons following evoked activation and its effects on the MR magnitude and phase. The theoretical simulation utilized real CA1 neuron morphologies of the rat hippocampus and determined the MR signal change within a 1.7 mm^3 volume of neurons. Both passive and active properties of real CA1 neurons were incorporated into the simulation to accurately calculate the resultant NMF and confirmed with magnetoencephalographic literature. CA1 neuron activation was initiated by AMPA-like currents of the oblique dendrites in order to approximate evoked input from the Schaffer collaterals. The approach of the Cassarà study to use authentic experimental measurements of CA1 neurons (Migliore, Ferrante et al. 2005) to theoretically predict the MR signal changes from a population of neurons gives confidence that the simulated predictions are accurate.

The purpose of this study was to evaluate the feasibility of the direct detection of evoked CA1 NMFs following stimulation of the Schaffer collaterals in the rat hippocampal slice. Simultaneous field potential recordings in the CA1 stratum pyramidale and MRS were used to evaluate the direct detection of a single evoked neural event. The stimulation to the Schaffer collaterals produced neuron activity of three forms: fiber volley of the Schaffer collateral action potentials, excitatory post-synaptic potentials of the CA1 dendrites and the population action potential spike from the CA1 axons (Bortolotto, Anderson et al. 2001).

Results of the simultaneous field potential recording and MRS control experiment were compared with the theoretically predicted results of Cassarà, Hagberg et al. (2008). The detection threshold for this experimental method was 25-100 times above the predicted phase change associated with activation of a similar CA1 hippocampal volume. It was not feasible under the current experimental conditions to measure the effects of evoked hippocampal activity using our MR methods.

3-3 Materials and Methods

3-3.1 Rat Brain Isolation and Preparation. Male, p10-p17 Sprague-Dawley rat pups (*Rattus norvegicus*, Charles River Laboratories, Wilmington, MA) were anesthetized with vaporized isoflurane for 2 min, or until the rat pup lost consciousness and maintained a slow and deep breathing pattern. The rat pup was immediately decapitated with a guillotine and the brain was removed from the skull. The isolated brain was transferred to 20 mL of 4°C cutting ACSF (85 mM NaCl, 2.5 mM KCl, 4.5 mM $MgSO_4$, 0.5 mM $CaCl_2$, 1.25 mM NaH_2PO_4, 25 mM $NaHCO_3$, 25 mM glucose, 75 mM sucrose, 300-320 mOsm and 7.4 pH) for 1 min. The cutting ACSF was maintained at 4°C by submerging the ACSF container in an ice water bath. All ACSF solutions were continuously aerated with a mixture of 95% O_2 and 5% CO_2 (NexAir, Suwanee, GA) to oxygenate and buffer the ACSF, respectively. Following 1 min, the isolated brain was transferred to 20 mL of fresh cutting 4°C ACSF and the following sections of the brain were removed with a

0.009 in. single edge razor blade: whole cerebellum, coronal section of the frontal cortex 3 mm caudal to the rostral tip of the olfactory bulbs and a 0.5 mm horizontal section from the dorsal surface of the cerebral cortex. The prepared brain was dried of excess ACSF and was fixed to the slicing platform with cyanoacrylate (Caliber liquid super glue, CVS Pharmacy, Woonsocket, RI). The previously cut dorsal surface of the cortex was fixed to the slicing platform with the ventral brain in the up position.

3-3.2 Hippocampal Slice Preparation. The brain and slicing platform were submerged in fresh 4^{o}C cutting ACSF and continuously aerated with a 95% O_2 and 5% CO_2 gas mixture. A vibrating-blade microtome (Leica VT 1000S, Nussloch, Germany) equipped with a stainless steel blade (double edge, CVS Pharmacy) cut the brain into 350 μm thick horizontal sections beginning with the ventral surface of the brain and proceeding dorsally. Individual brain slices were cut in the rostral to caudal direction and the two hemispheres were separated with a 25G 5/8 hypodermic needle (Becton Dickenson and Company, Franklin Lakes, NJ) that was bent 90^{o} and acted as a blade. Each individual brain slice provided two hippocampal slices, one from each hemisphere. The hippocampal slices were transferred to the slice-incubation chamber that contained 150 mL of normal ACSF (119 mM NaCl, 3.0 mM KCl, 1.2 mM $MgSO_4$, 1.2 mM $CaCl_2$, 1.0 mM NaH_2PO_4, 26 mM $NaHCO_3$, 10 mM glucose, 280-300 mOsm and 7.4 pH), was aerated with the 95% O_2 and 5% CO_2 gas mixture and was incubated at 22^{o}C (room temperature) for 1 hr before experimentation (Reid, Edmonds et al. 1988; Madison and Edson 1997).

3-3.3 Electrodes and Electrophysiological Equipment. Glass recording electrodes were manufactured by pulling borosilicate glass capillaries with filaments (outer diameter = 1.50 mm, inner diameter = 1.17 mm, length = 7.5 cm) (Warner Instruments, LLC, Hamden, CT) using a single stage glass microelectrode puller (model PP-830, Narishige Group, Japan). The electrode tip was marked with black India ink (Speedball, Statesville, NC) and the ink was fixed to the glass with a hot air dryer. The electrode was filled with ACSF via the open end of the capillary. The electrode tip was carefully broken to produce an electrode impedance of <3 MΩ.

A silver chloride (AgCl) wire was inserted into the open capillary end of the glass recording electrode to make electrical contact with the ACSF. An AgCl reference wire was placed in the bath of the slice recording chamber 1 cm from the slice. The recording electrode and reference wire measured the extracellular field potential differentially (Differential AC Amplifier, Model 1700, A-M Systems, Sequim, WA) and was digitized by a Digidata 1320A (Axon Instruments, Sunnyvale, CA). Clampex 9.2 software (Axon Instruments) stored the amplified, filtered and digitized electrophysiological time courses.

3-3.4 Field Recordings of Spontaneous CA1 Activity. The hippocampal slice was placed in a submergence recording chamber with the perfusion of ACSF over the single, top surface of the slice at a rate of 2.0 mL/min using a Minipuls 3 peristaltic pump (Gilson, Inc., Middleton, WI). ACSF was aerated with a 95% O_2 and 5% CO_2 gas mixture and heated to 32-34°C using a TC-344A Dual Heater

Controller (Warner Instruments). The hippocampal slice was perfused with seizure ACSF (119 mM NaCl, 8.5 mM KCl, 1.2 mM $MgSO_4$, 1.2 mM $CaCl_2$, 1.0 mM NaH_2PO_4, 26 mM $NaHCO_3$, 10 mM glucose, 280-300 mOsm and 7.4 pH) in the experimental condition and with normal ACSF in the control condition.

Recording electrode tips located in the stratum radiatum or stratum pyramidale of the CA1 region of the hippocampus recorded spontaneous field potentials. The following parameters were used during measurement of the spontaneous hippocampal field potentials: gap-free acquisition mode, 10 kHz sampling bandwidth, 10-60 min experimental trial duration, 1 kHz low-pass filter and 10 Hz high-pass filter.

3-3.5 Field Recordings of Evoked CA1 Activity. The hippocampal slice was placed in a submergence recording chamber with the perfusion of excitatory ACSF (119 mM NaCl, 3.0 mM KCl, 1.5 mM $MgSO_4$, 2.5 mM $CaCl_2$, 1.0 mM NaH_2PO_4, 26 mM $NaHCO_3$, 10 mM glucose, 280-300 mOsm and 7.4 pH) over the single, top surface of the slice at a rate of 2.0 mL/min. The excitatory ACSF was aerated with the 95% O_2 and 5% CO_2 gas mixture and heated to 32-34^{o}C.

The tip of a glass recording electrode was located to the stratum pyramidale of the CA1 region of the hippocampus. The following parameters were used during measurement of the evoked hippocampal field potentials: episodic stimulation acquisition mode, 20-1,000 repetitions per trial, 10 kHz sampling bandwidth, 100 ms sampling duration, 3 s inter-stimulus interval, 1 kHz low-pass filter and 10 Hz high-pass filter.

The negative terminal of a Pt/Ir stimulating microelectrode <1 MΩ (FHC Inc., Bowdoin, ME) was located to the Schaffer collaterals of the CA1 stratum radiatum of the hippocampus and the positive terminal was connected to the ACSF bath reference wire. A pulse generator (Master-8, A.M.P.I., Jerusalem, Israel) initiated a stimulus pulse with a 5.0 ms delay and 0.3 ms width. The amplitude of the stimulation pulse was controlled by a stimulus isolator (A360 stimulus isolator, World Precision Instruments, Sarasota, FL) and was varied between 80 and 250 μA until evoked activity was recorded.

3-3.6 Manufacture of Radio-Frequency Microcoils and Circuit Boards. The radio-frequency (RF) microcoil was manufactured in a microelectromechanical laboratory (Florian Herrault, PhD, Georgia Institute of Technology) and mimicked previously reported dimensions (Fig. 3-1) (Massin, Boero et al. 2002; Eroglu, Gimi et al. 2003; Massin, Vincent et al. 2003; Webb 2005; Ehrmann, Gersbach et al. 2006). The coils were fabricated on the surface of either a silicon or a glass substrate and contained two copper layers. The initial 15 μm thick copper layer was electrodeposited into a photoresist mold (NR9-8000 P, Futurrex) that was in the shape of the first layer of the coil. An electrically insulating layer of SU-8 was spin coated on the first copper layer and via holes were opened in the SU-8. These holes in the SU-8 insulation permitted electrical connections to be made between the first and second copper layers at specific points of the microcoil and for all other points of the copper layers to be electrically insulated. The second 15 μm thick copper layer was electroplated over the SU-8 layer through the second photoresist mold. Copper was electroplated through the via holes to form electrical connections between the top and bottom copper layers. The top copper conductor layer was coated with a 5 μm thick layer of parylene, a thin vapor-deposited insulating material (Herrault, Chang-Hyeon et al. 2008; Herrault, Yorish et al. 2010). The RF microcoil was the site of the FID acquisition (Fig. 3-1).

The coil circuit board was constructed from copper-clad (single-side) Grade G-10/FR4 Garolite (1/32 in. thickness) (McMaster-Carr, Robbinsville, NJ). The copper surface of the circuit board was minimized to compactly fit the required electronic components and to minimize the transmission and receiving of radio frequencies by the circuit board. Tuning and matching 0.5-8 pF surface mount non-magnetic trimmer capacitors (NMA1J8HV, Voltronics Corporation, Denville, NJ) and a 13 pF non-magnetic chip center capacitor (11-13-J-1000-W-H, Voltronics Corporation) were used in the design of the circuit (Fig. 3-2A). A dual PHEMT RF preamplifier tuned to the resonant frequency amplified the received FID signal (Angle Linear, Lomita, CA). Odd and even multiples of the coaxial cable (Type 9223, Belden Inc., Richmond, IN) quarter wavelengths (λ/4) minimized power transmission at the RF preamplifier and maximized the power transmission at the microcoil during the spin excitation pulse, respectively. A coaxial cable length of 6.7 cm (1λ/4) connected the Y-splitter to the input terminal of the RF preamplifier to safely activate the internal anti-parallel diodes and to prevent a destructive power surge at the preamplifier. A coaxial cable length of 17.2 cm (2λ/4) connected the Y-splitter to the coil circuit board to maximize the transmitted excitation power to the microcoil (Fig 3-2B). The quarter wavelength calculation:

$$\frac{n\lambda}{4} = \frac{cnV_f}{4f_r} \quad \textbf{Eq. 3-1}$$

Where λ is the wavelength, n is the wavelength multiple, c is the speed of light, V_f is the velocity factor of the coaxial cable (56%, Type 9223, Belden Inc.) and f_r is the resonant frequency (400.3 MHz). The velocity factor was assumed to be equal to that of the coaxial cable when considering lengths contributed by the Y-splitter, coil circuit board and RF preamplifier.

3-3.7 Chamber Allowing Simultaneous Field Potential Recordings and MRS. The chamber allowing simultaneous field potentials and MRS was constructed of a single compartment. The micro-machined RF coil was fixed to the center of a rigid acrylic base (6.5 cm x 21.0 cm x 0.6 cm) with Mighty Putty (Plymouth Direct, Inc., Montgomeryville, PA). Care was taken to fix the height of the coil to the same height as the base of the chamber (0.2 cm). Excess Mighty Putty was removed from the four sides of the coil and was permitted to dry for 12 hr. The parylene film over the coil solder pads was gently removed with a scalpel and cleaned with ethanol. The pre-manufactured RF circuit board and coaxial cable were mechanically fixed to the acrylic base using super glue, Mighty Putty and hot glue. The circuit board and all of its pre-soldered components were mechanically stable to ensure that the solder points between the microcoil and RF circuit board could not break during the tuning and matching of the coil. A 3 mm length of 30-gauge copper magnet wire (RadioShack Corporation, Fort

Worth, TX) was soldered to the RF circuit board and coil solder pads at 500°F. A layer of cyanoacrylate was applied to the solder points to mechanically secure the RF circuit board to the microcoil.

Custom acrylic pieces (0.2 cm thickness) were used to construct the raised floor and the four chamber walls with the following dimensions: 3.6 cm x 1.7 cm x 1.3 cm. Each of the two longest lengths of the chamber wall was modified to suit the experimental methods. First, the wall height opposite of the coil was reduced to 0.4 cm to allow for the electrophysiological electrodes to be angled into the hippocampal tissue. The tissue was placed directly on the microcoil surface. Second, the base of the wall that rested over the coil was notched to allow space for the coil solder points. 100% clear silicone rubber (Dow Corning Corporation, Midland, MI) sealed the chamber walls and electrically insulated the exposed coil solder points. Inlet and outlet R-3603 Tygon perfusion tubing (0.16 cm inner diameter, 0.32 cm outer diameter) (Saint-Gobain Performance Plastics Corporation, Akron, OH) were fixed to opposite sides of the chamber at the maximum distance allowed. The inlet tube was connected to a peristaltic pump and brought fresh ACSF into the simultaneous chamber, while the outlet tube was connected to a vacuum pump and removed waste ACSF from the chamber. A bead thermistor (TS-70B, Warner Instruments) and a silver chloride (AgCl) reference wire were fixed to the floor of the chamber half way between the inlet tube and the microcoil. The thermistor continuously monitored the temperature of the heated ACSF. The electrode platform was an acrylic tower that supported an angled glass slide and was fixed to the acrylic base opposite to the microcoil. This platform secured the recording and stimulating microelectrodes in a fixed position for electrophysiological measurements in the absence of the micromanipulators. The steel micromanipulators were removed from the chamber after the electrodes were fixed to the angled glass slide of the electrode platform. The electrode platform was fixed once the electrode rested on the glass slide and had its tip just above the microcoil center. The completed chamber was permitted to dry for 12 hr (Fig. 3-3).

3-3.8 Tuning, Matching and Quality Factor of the Microcoil. The chamber containing the microcoil was filled with an ACSF load and tuned to 400.3 MHz (resonant frequency, f_r) and matched to 50 Ω with a 8753D Network Analyzer (Hewlett-Packard Company, Palo Alto, CA). The frequency bandwidths (Δf) at 250 and 500 mU were measured and the quality factor (Q) calculated for each bandwidth:

$$Q = \frac{f_r}{\Delta f}$$ **Eq. 3-2**

3-3.9 Calculating B_0 Phase Difference Maps. The phase difference map of B_0 was required to determine the level of B_0 distortion caused by the magnetic susceptibility of the microcoil substrate materials. Experiment 1 measured the B_0 field distortion caused by a microcoil constructed on a silicon substrate against a microcoil (chemically removed from it substrate) fixed to an acrylic substrate with scotch tape. Experiment 2 measured the B_0 distortion caused by a microcoil manufactured on a silicon substrate against one on a glass substrate.

A water phantom was constructed to contain the substrates. The phantom base was solid 1% agarose in double distilled ($_{dd}$)H_2O, on which the substrate was placed, and the remaining volume was filled with liquid $_{dd}H_2O$. The water phantom was located to the center of an RF volume coil, tuned to 400.3 MHz and matched to 50 Ω. The static magnetic field (B_0) was automatically shimmed and the resonant frequency was adjusted to minimize off-resonant effects. The following parameter were used: MGE-T2star-map acquisition mode, 1,000 ms T_R, 2 echoes, 4.89 ms T_{E1}, 12.67 ms T_{E2}, 512 x 512 matrix, 30.5 mm x 30.5 mm isotropic field of view, 1.0 mm slice thickness, 1 saggital slice (orientation parallel to B_0) and 5 dummy scans.

One image was acquired during each of the two echo times. The images contained both the real and imaginary components of the signal and allowed for calculation of phase images. The phase difference map was determined by subtracting the T_{E2} from the T_{E1} phase image.

3-3.10 Calculating the Microcoil Signal-to-Noise Ratio and Signal Decay Time. The signal-to-noise ratio (SNR) and signal decay time (T_2*) were calculated from an experimentally acquired FID. The simultaneous chamber was filled with ACSF and the microcoil was tuned to 400.3 MHz, matched to 50 Ω and located to the isocenter of the 9.4 T. B_0 was automatically shimmed and the resonant frequency was adjusted to minimize off-resonant effects. The FID was measured with the following parameters: singlepulse acquisition mode, 1,638.4 ms acquisition time, 3.125 kHz sampling frequency, 5,120 points acquired, 2,000 ms T_R, 10 dummy scans, 20 repetitions, a bp32 excitation pulse shape and a 0.1

ms excitation pulse duration. The mean of the 20 FID repetitions was determined and the magnitude component of the average FID was calculated. The SNR was calculated using the FID magnitude at t = 0 ms (M_{max}) and the root mean square of the final 100 magnitude points according to the following equation:

$$\mathrm{SNR} = {}^{\mathrm{M_{max}}}\Big/_{2 * \sqrt{\frac{\sum_{n-99}^{n} M_n^2}{100}}} \qquad \textbf{Eq. 3-3}$$

Where n is the final magnitude point that was sampled (n = 5,120).

The T_2^* of the FID magnitude was also calculated. An exponential decay curve was best fit to the discretely sampled FID magnitude points. The time at which 63.2% of M_{max} had decayed was equal to T_2^* by to the following equation:

$$\mathrm{M(t)} = \mathrm{M_{max}} * (1 - \mathrm{e}^{t/T_2^*}) \qquad \textbf{Eq. 3-4}$$

A larger value of T_2^* signified a slower exponential decay of the FID in time, which increased the time span that the FID could be measured before the signal reached zero.

3-3.11 Determining the Microcoil Excitation Power. Different power intensities were applied to the microcoil excitation pulse to determine the intensity at which a maximal signal was recorded. The simultaneous chamber was filled with ACSF and the microcoil was tuned to 400.3 MHz, matched to 50

Ω and located to the isocenter of the 9.4 T. B_0 was automatically shimmed and the resonant frequency was adjusted to minimize off-resonant effects. The following parameters were used in the acquisition of the FLASH images: 5.958 ms echo time (T_E), 200 ms T_R, 8 averages, the transmission power attenuation for the excitation pulse was varied between 35 and 80 dB, bp32 excitation pulse shape, 0.1 ms excitation pulse duration, 256 x 256 matrix, 5.0 mm x 5.0 mm isometric field of view, 0.778 mm slice thickness, 3 axial slices (orientation perpendicular to B_0) and 30 dummy scans.

The volume of space above the surface microcoil in which the hippocampal slice occupied was analyzed. A rectangular region of interest (ROI) was selected that corresponded to the inner diameter of the microcoil and the thickness of the hippocampal slice (1.00 mm x 0.35 mm). The magnitude of each voxel contained in the ROI was calculated and averaged. The averaged magnitude values were calculated for each transmission power to determine the power level necessary to maximize the magnitude signal in the volume that the hippocampal slice occupied.

3-3.12 Simultaneous Field Recording Acquisition. The method to record field recordings was previously described in section "3-3.5 Preliminary Field Recordings of Evoked CA1 Activity". Hippocampal slices were prepared, submerged in the normal ACSF of the slice incubation chamber and sealed in a desiccator during the 1-hr incubation period. During this time, the 95% O_2 and 5% CO_2 gas mixture aerated the normal ACSF and saturated the desiccator atmosphere with oxygen gas. The saturated oxygen gas atmosphere surrounding the slices was preserved for the 7 min walk from the slice preparation room to the location of field potential recordings at the 9.4 T. A latex balloon filled with a 95% O_2 and 5% CO_2 gas mixture replaced the immobile gas mixture cylinder and permitted aeration of the normal ACSF during the 7 min. The desiccator and latex balloon maintained a high level of dissolved oxygen in the normal ACSF during the transfer of the slices from the location of slice preparation to the 9.4 T.

A glass stimulating electrode replaced the Pt/Ir stimulating microelectrode and was placed in the stratum radiatum (Fig. 3-4). Both positioned stimulating and recording glass electrodes were secured to the glass slide of the electrode platform using cyanoacrylate. The steel micromanipulators were removed from the electrodes after 15 min to allow for the cyanoacrylate to cure. The electrophysiological, perfusion and temperature sensor lines were disconnected from the chamber and relocated to the 9.4 T. Additional electrophysiological, perfusion and temperature sensor lines, which were located in the 9.4 T, were immediately reconnected to the chamber. The length of the additional perfusion and electrical lines were greater than 3 m to separate the ferro-magnetic equipment from the 9.4 T magnet.

Both the electrophysiological digitizer and the stimulation of the hippocampal slice were initiated by the TestCur2 MRS protocol during even T_Rs. The stimulus pulse had a 5.0 ms delay, 0.3 ms width and 232 μA amplitude (Fig. 3-5). The following parameters were used to measure the evoked hippocampal field potentials: episodic stimulation acquisition mode, 1,000 repetitions per trial, 10 kHz sampling bandwidth, 2.064 s sampling duration, 4 s inter-stimulus interval, 100 gain, 1 kHz low-pass filter and 10 Hz high-pass filter.

3-3.13 Simultaneous MRS Acquisition. The microcoil was tuned to 400.3 MHz, matched to 50 Ω and the simultaneous chamber was located to the isocenter of a 9.4 T Bruker Biospin after all perfusion and electrophysiological lines were connected. The excitatory ACSF perfusion was replaced by $_{dd}H_2O$ for 5 min in the control condition and permanently terminated activity from the hippocampal slice. The slice was destroyed to assess the MRS detection threshold. Excitatory ACSF perfusion was resumed before the acquisition of any FID time courses. B_0 was automatically shimmed and the resonant frequency was adjusted to minimize off-resonant effects. The following parameters were used: TestCur2 acquisition mode, 3.125 kHz FID sampling bandwidth, 81.92 ms acquisition time, 256 quadrature detected time points, 56 dB excitation transmission attenuation, 2.0 s repetition time (T_R), 2,000 repetitions per trial and 6 dummy scans. The MRS experiment was controlled by ParaVision 4.0 (Bruker Biospin). Each experiment lasted 5-6 hr.

The transmit and receive microcoil used quadrature detection to simultaneously acquire the real and imaginary components of the FID. During odd T_R's, the MRS protocol was initiated without triggering the current stimulation of the hippocampal slice. This group was used in post-processing steps to correct for FID phase drift. During even T_R's, the hippocampal slice was stimulated at 232 μA. The FID excitation pulse was initiated 0.1 ms after the stimulation at the hippocampal slice had ceased (Fig. 3-5). No magnetic field gradients were used during the experiment and only data from the control hippocampal slice were collected.

3-3.14 Data Analysis – Simultaneous Electrophysiology. Field potentials were acquired from the recording electrode for every T_R. Using Clampfit 9.2 (Axon Instruments), each repetition was separated into the components that corresponded to the even and odd T_Rs. The absence of the stimulation artifact was verified in the odd T_R group and was not used for further analysis. The baseline for each trace was corrected to zero and the absence of hippocampal slice activity was verified for each individual trace that corresponded to an even T_R. Finally, the mean field potential for even T_Rs was calculated.

3-3.15 Data Analysis – Simultaneous MRS. The interleaved MRS time courses were separated into odd and even T_R groups. The phase information was processed by multiplying individual even T_R FIDs by the complex conjugate of the preceding odd T_R FID. The phase of the FID was calculated and filtered (4th order, Type 1 Chebyshev, 200 Hz high-pass filter) (Matlab R2007a, The MathWorks, Inc., Natick, MA). The mean of the individually prepared FIDs was calculated.

3-3.16 Modeled MR Magnitude and Phase Change. The magnitude and phase change associated with evoked NMFs from the CA1 region of the hippocampus was previously modeled (Cassarà, Hagberg et al. 2008). The results that were relevant to our experiment were analyzed to determine the detection threshold of our methods. Welch power spectral density estimates for the predicted phase time courses (z-orientation) were calculated. The phase time courses were also filtered with the identical Type 1 Chebyshev 200 Hz high-pass filter that was applied to the experimentally acquired FIDs and Welch power spectra of the filtered phase data were calculated.

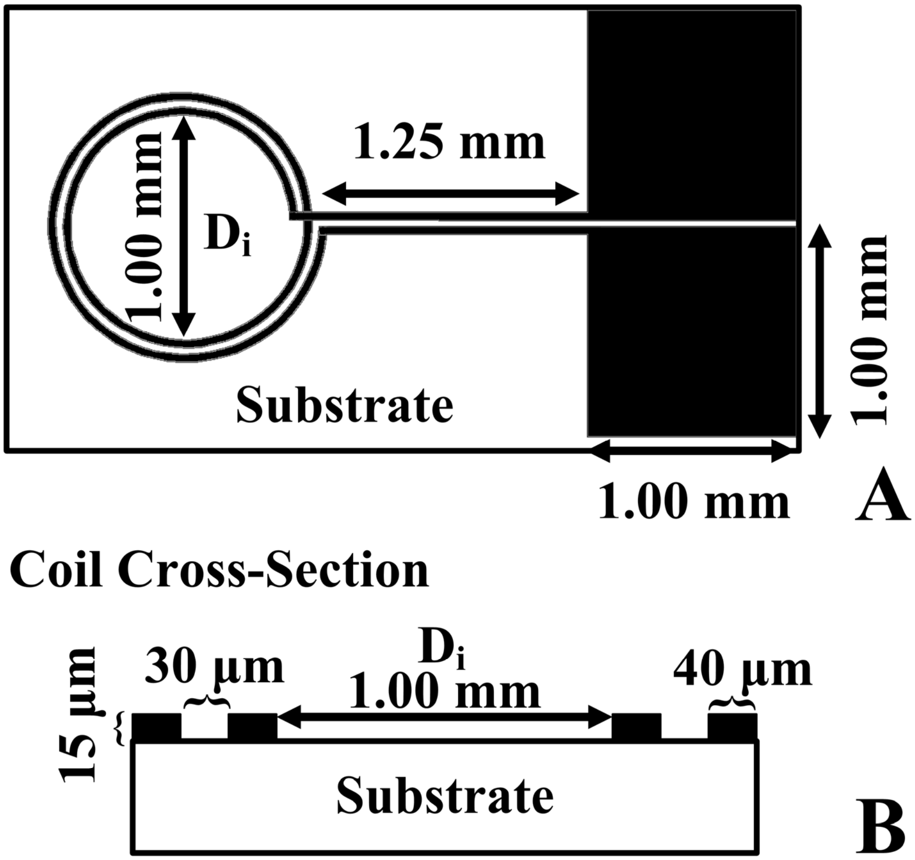

Figure 3-1 Surface RF Microcoil: The RF surface microcoil for the hippocampal slice was produced using micromachine and photolithographic techniques on silicon and glass substrates. The hippocampal slice was located directly on the surface of the circular region of the coil. The finished coil had two turns of copper and an inner diameter of 1.00 mm (D_i). The coil was linked to the 1.00 mm^2 solder pads by 1.25 mm copper traces. The solder pads were the points of connection of the coil to the coil circuit board (A). A cross-section of the circular coil details the dimensions of the copper traces (trace thickness = 150 µm, trace width = 40 µm and inter-trace spacing = 30 µm).

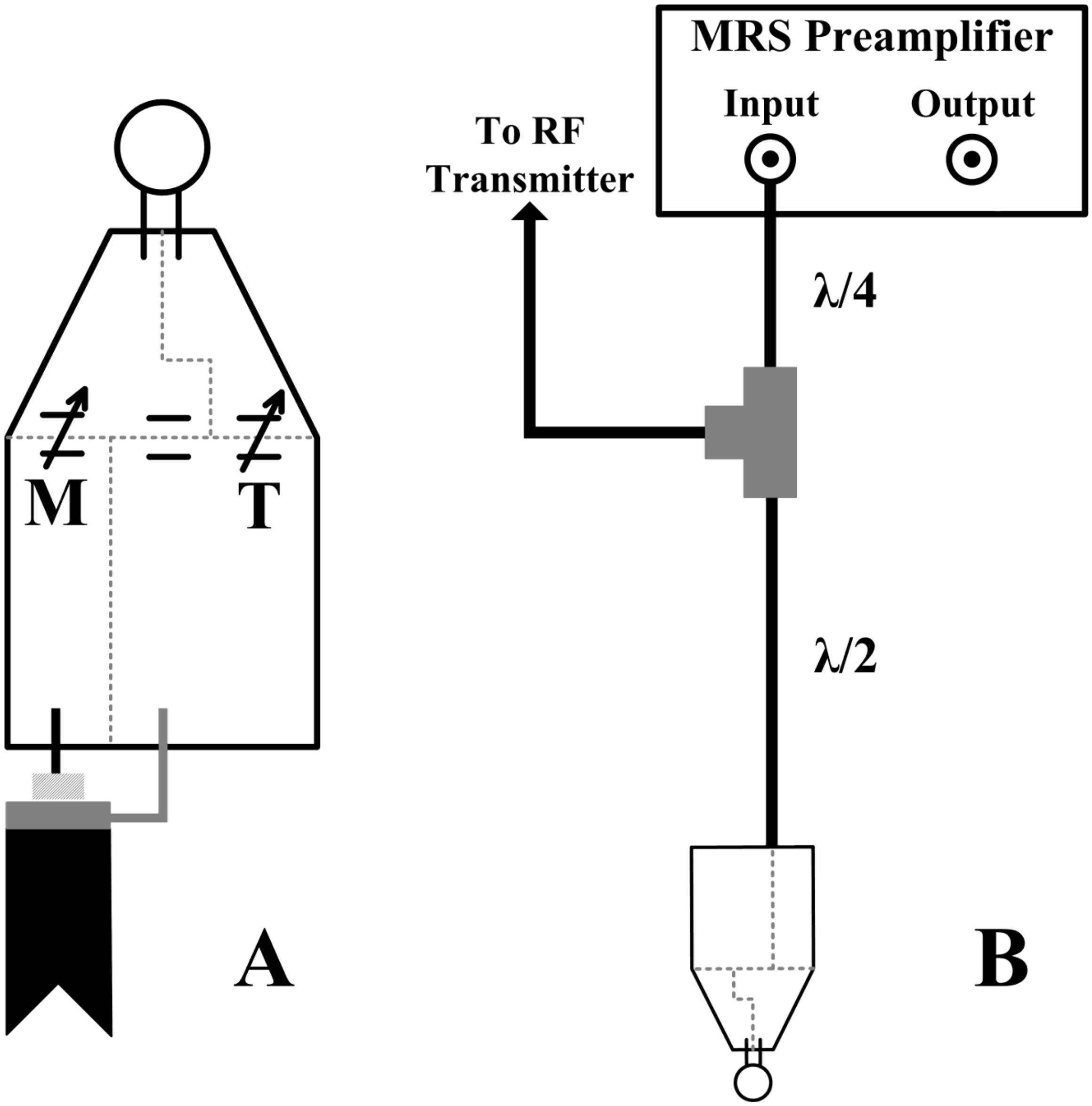

Figure 3-2 Coil Circuit Board and Connections to the RF Transmission Line and MRS Preamplifier: The coil circuit contained one tuning (T) and one matching (M) trimmer capacitor in parallel with the coil and a single constant chip capacitor in series with the coil. Dotted gray lines (---) represent lines in which the copper plating was etched away (A). The transmission line was connected to the MRS preamplifier by λ/4 coaxial cable in order for the diodes to activate during spin excitation and prevent damage to the preamplifier (B).

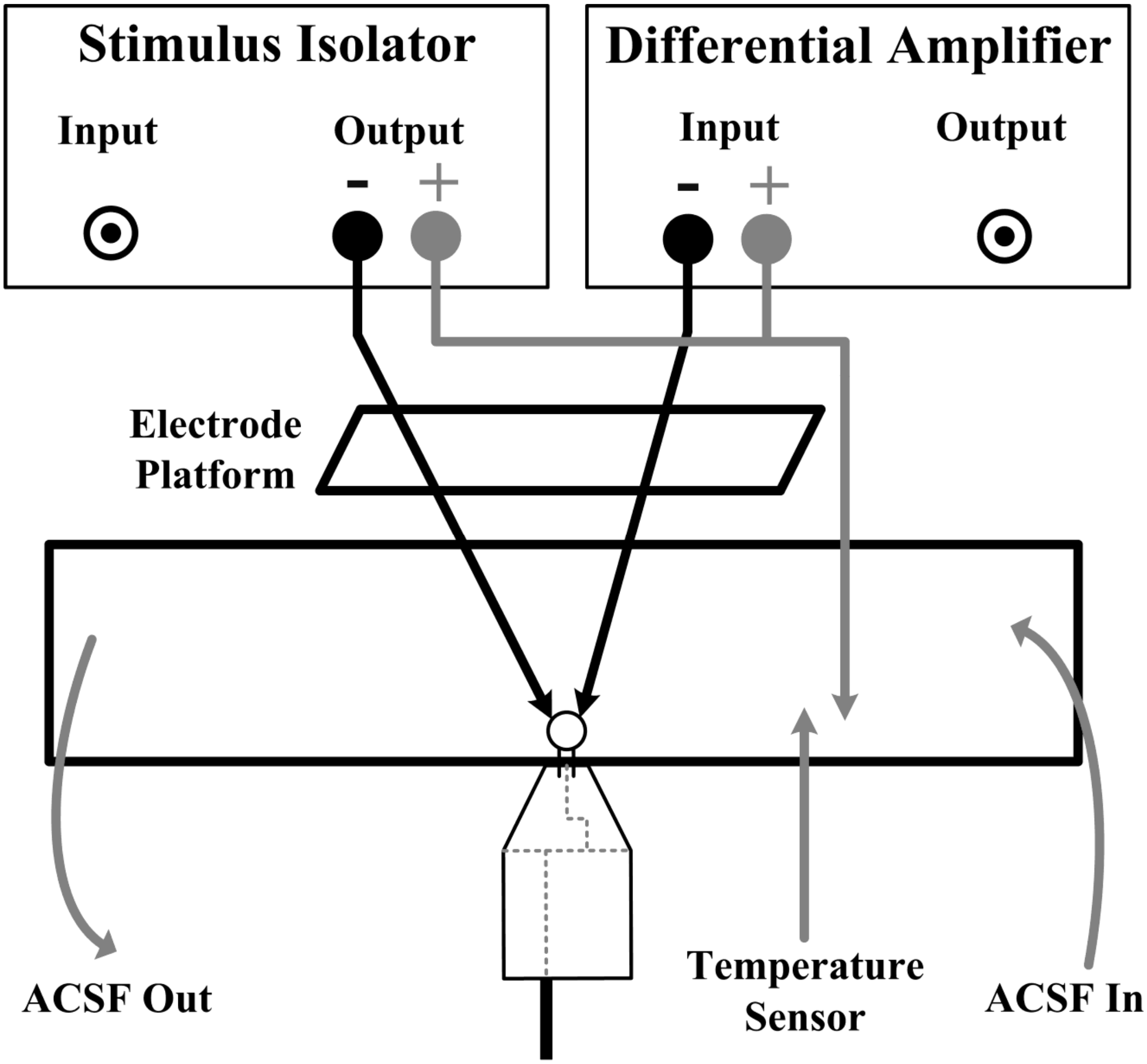

Figure 3-3 Chamber Allowing Simultaneous Field Potential Recordings and MRS for the Hippocampal Slice: The hippocampal slice was located directly above the surface of the RF microcoil. Heated and aerated ACSF was pumped into the chamber and flowed over the single, top surface of the slice. The temperature of the bath was measured between the ACSF inlet and mircocoil. Stimulating and recording electrodes were located to the CA1 region of the hippocampal slice with the use of micromanipulators. The wall opposite to the coil was reduced in height to give the electrodes access to the hippocampal tissue. The electrodes were fixed to the electrode platform with cyanoacrylate and

the steel micromanipulators were removed from the experiment before the chamber was relocated to the 9.4 T. Field potentials were recorded differentially with reference to the ground electrode located in the ACSF bath. The ground electrode was shared with the positive terminal of the stimulating electrode.

Figure 3-4 Photograph of the simultaneous hippocampal field recording and MRS experiment: The surface microcoil is located at the top of the photo and the hippocampal slice is located at the bottom. The Pt/Ir stimulating and glass recording electrodes were positioned in the stratum radiatum of the CA1 region of the hippocampus. The CA1 region was placed directly on the surface of the microcoil during the simultaneous experiment.

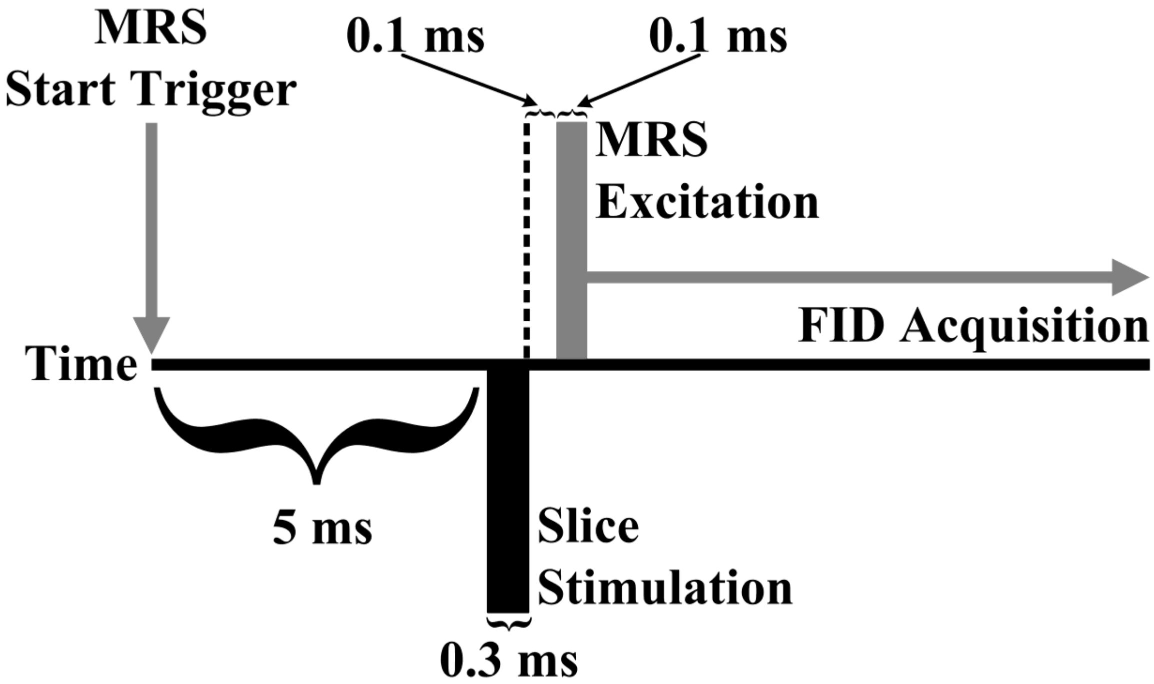

Figure 3-5 Timing of the Simultaneous Field Potential Recordings and MRS Experiment: During even T_Rs, TestCur2 MRS acquisition method initiated a trigger to stimulate the hippocampal slice. The stimulus was delayed 5 ms after the trigger and had a temporal width of 0.3 ms. The MRS excitation pulse to the RF microcoil followed 0.1 ms after the cessation of the slice stimulus and the FID time course was acquired. During odd T_Rs, there was no electrical stimulation of the hippocampal slice, but all other MRS timings schemes were identical. Odd T_Rs were used in post-analysis steps to correct for phase drift.

3-4 Results

3-4.1 Preliminary Field Potential Recordings. Spontaneous activity was elicited from the hippocampal slice by increasing the extracellular potassium ion concentration in the ACSF medium from 3.0 to 8.5 mM. The activity ceased with the return of the potassium ion concentration to normal. Field potentials varied in direction (positive or negative voltage spikes), amplitude and time between subsequent events during the course of the spontaneous activity (Fig. 3-6A).

Evoked activity was elicited from the hippocampal slice by stimulating the Schaffer collaterals and measuring the resultant field potential at the CA1 pyramidal cell bodies. The action potential fiber volley that originated from the Schaffer collaterals was recorded before the excitatory post-synaptic potential (EPSP). The EPSP peak amplitude was increased by the application of a stronger current stimulus to the Schaffer collaterals. A population spike originating from the CA1 pyramidal neurons resulted with the continued increase of the applied stimulus. These three types of field potential recordings (fiber volley, EPSP and population spike) had a consistent amplitude, duration and timing following the Schaffer collateral stimulation. The maximum amplitude of the evoked field potentials was generally less than the peak spontaneous potentials (Fig. 3-6B).

3-4.2 Phase Difference Maps. Experiment 1 compared the coil on a silicon substrate (Fig. 3-7A) to a substrate-free coil that was fixed to an acrylic base with scotch tape (Fig. 3-7B). The coil fixed to the acrylic base was chemically removed from its silicon substrate and, therefore, lost its functionality. The acrylic substrate did not distort the B_0 magnetic field while the copper coil was observed to slightly distort it. The distortion was characterized by a difference of two phase images that were measured 7.78 ms apart. Trapped air around the edges of the coil and the scotch tape could have resulted in the susceptibility difference observed at the location of the coil (Fig. 3-7B). The copper coil on silicon substrate had a very significant distortion of B_0. The phase changed 9.4 radians along the axis of the coil to -5 mm on the Y-axis (Fig. 3-7A). The coil axis was defined as the line drawn perpendicular to the substrate surface and parallel to the Y-axis that begins at the substrate center.

Experiment 2 compared the distortion of B_0 that resulted from the microcoil on silicon (Fig. 3-7C) and glass substrates (Fig. 3-7D). The method to measure the phase difference maps of the silicon substrate was identical for Experiments 1 and 2. The repetition was necessary because Experiments 1 and 2 occurred on different days. The phase along the coil axis changed 8.6 radians along the axis of the coil to -5 mm on the Y-axis for the silicon substrate (Fig. 3-7C), while the glass substrate changed 5.3 radians (Fig. 3-7D).

3-4.3 Free-Induction Decay SNR and T_2*: The SNR and T_2* were calculated for microcoils on silicon and glass substrates. Measurements from each microcoil type used in this analysis had the following criteria: 50-57 dB transmission excitation power attenuation, 3,125 Hz FID sampling bandwidth and 1,638.4 ms acquisition time. The SNR and T_2* for the silicon microcoil were 466.6 ± 77.7 and 2.9 ± 0.6 ms (*M* ± *SD*), respectively, (n = 7); compared to 1,324.1 ± 214.4 and 9.0 ± 1.1 ms (n = 34) for the glass microcoil. The glass microcoil had a 184% increase in the mean SNR and a 210% increase in the mean T_2^* compared to the silicon microcoil (Fig. 3-8).

3-4.4 Microcoil Excitation Power. Optimization of the transmission power to the RF microcoil was necessary to maximize the signal in the sensitive region of the coil occupied by the hippocampal slice. A plot of the excitation power attenuation and the average magnitude signal in the hippocampal slice volume showed a parabolic response with the optimal power attenuation located at the peak of the parabola. The optimal power attenuation was measured at 52, 56, 56 and 57 dB for four different microcoils on glass substrate (Fig. 3-9).

3-4.5 Simultaneous Field Potential Recordings and MRS in the Hippocampal Slice: Five trials with 4,985 processed phase time courses were acquired during a 6 hr experiment in the control hippocampus. The average SNR and T_2^* of the experiment was 1,120 ± 20 and 8.6 ± 0.3 ms, respectively. An 8-ms window was chosen for all measured phase FID analyses since this duration represented the majority of the signal envelope as defined by the average T_2^*.

The Welch power spectral density estimate for the mean control phase time course revealed a dominant low frequency component in the 0 – 100 Hz range with an amplitude of $0.1 - 3.0 \times 10^{-6}$ arbitrary units (a.u.) (Fig. 3-10a, black line). The control FID phase exhibited a low frequency drift in the time domain from 0 – 8 ms and had a maximum phase change of $\Delta 9.7 \times 10^{-4}$ radians during this time (Fig. 3-11A). The low frequency spectral component was eliminated by a 200 Hz, 4th order, Type 1 Chebyshev high-pass filter (Fig. 3-10b, black line).

The low frequency drift in the time domain was also eliminated and resulted in a maximum phase change of Δ6.0 x 10^{-5} from 0 – 8 ms (Fig. 3-11A).

Cassarà, Hagberg et al. (2008) simulated and reported the FID phase of a CA1 hippocampal volume following evoked activation. A Welch power spectral density estimate was calculated for their reported FID phase (neuron type 2, z-orientation) and this estimate showed a dominant low frequency component in the 0 – 100 Hz range with an amplitude of 0.1 – 1.5 x 10^{-12} a.u. (Fig. 3-10b, gray line). A low frequency drift was observed in the time domain of the reported phase and had a maximum phase change of Δ9.4 x 10^{-6} radians from 0 – 8 ms. The low frequency spectral component was eliminated by the 200 Hz high-pass filter (Fig. 3-10B, gray line), which also eliminated the low frequency drift in the time domain of the reported FID phase time course. Higher frequency components in the FID phase remained at the three moments corresponding to the evocation of the CA1 neurons. The maximum change in the FID phase after filtration was Δ2.2 x 10^{-6} radians from 0 – 8 ms (Fig. 3-11B).

The measured FID phase and simulated FID phase changes were compared (Fig. 3-11C). The simulated phase change (Δ9.4 x 10^{-6} radians) was approximately 100 times less than that of the control experiment (Δ9.7 x 10^{-4} radians) without application of the 200 Hz high-pass filter. Also, the simulated phase change (Δ2.2 x 10^{-6} radians) was approximately 25-times less than that of the control experiment (Δ6.0 x 10^{-5} radians) with application of the 200 Hz high-pass filter. The SEM (n = 4,985 phase time courses) was calculated for each of the high-pass filtered, control phase FID time points in the 0 – 8 ms range. The average SEM of these 26 time points was 2.6 x 10^{-5} radians.

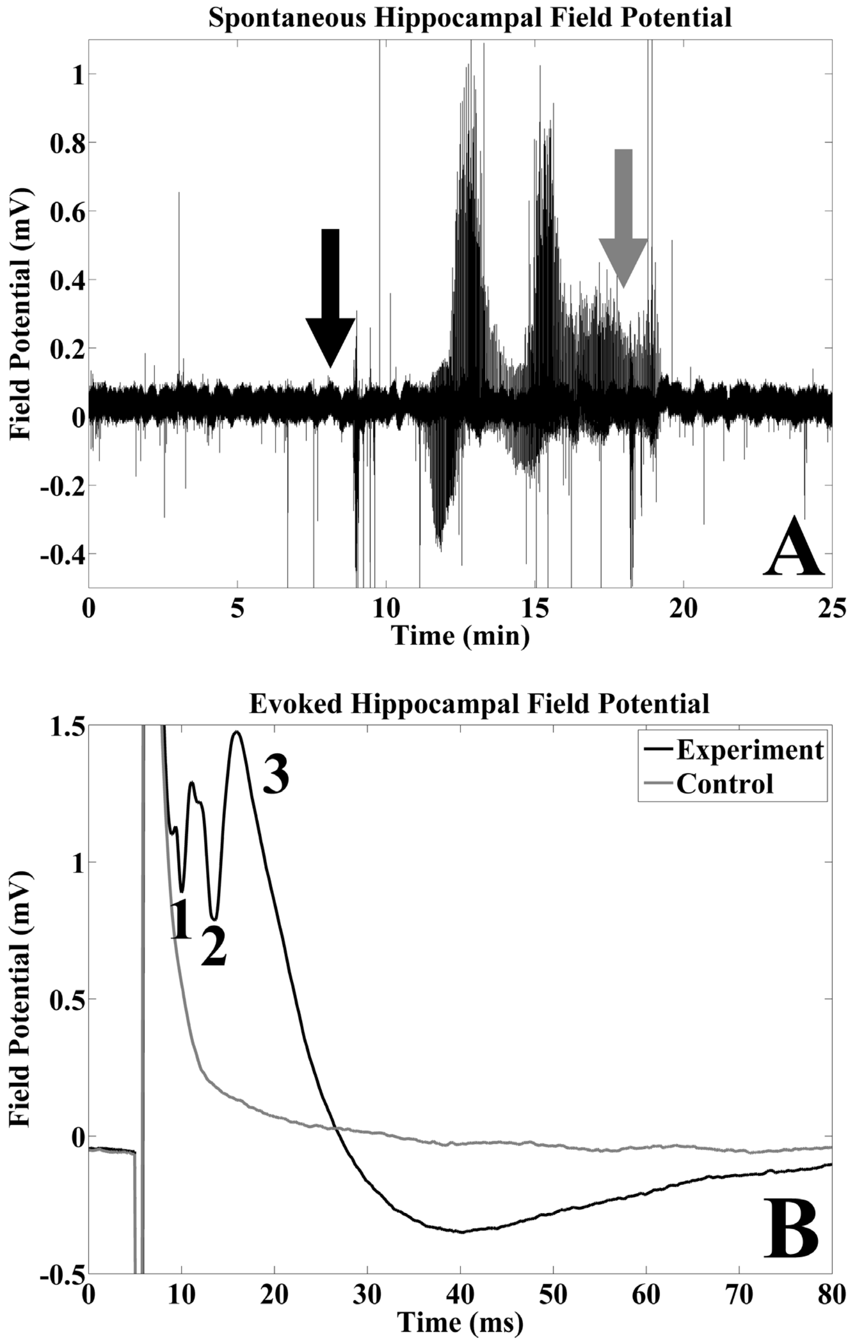

Figure 3-6 Spontaneous and Evoked Hippocampal Field Recordings: Preliminary results from a spontaneous (A) and an evoked (B) hippocampal field potential experiment. In the spontaneous experiment, the normal ACSF was replaced by seizure ACSF (black arrow). Spontaneous activity was recorded at the CA1 stratum radiatum shortly after the seizure ACSF filled the recording

chamber. The seizure ACSF was replaced by normal ACSF 10 min later (gray arrow) and the spontaneous activity ceased. The seizure ACSF contained a greater concentration of K^+ ions compared to the normal ACSF (3.0 mM to 8.5 mM). In the evoked experiment, the Pt/Ir stimulating electrode was located to the CA1 stratum radiatum and the glass electrode to the CA1 stratum pyramidale. A 220 μA current was injected into the tissue to stimulate the Schaffer collaterals. The resulting field potential contained the initial action potential fiber volley from the Schaffer collaterals (1), the population action potential spike from CA1 neurons (2) and the excitatory post-synaptic potential (EPSP) of CA1 dendrites (3) (solid black line – panel B). The initial phase of the EPSP recording occurred at a time simultaneous to the population spike and resulted in their overlap. The glass recording electrode tip was withdrawn to the surface of the hippocampal slice and out of the tissue in the control condition (gray line). The control field potential contained only the stimulation artifact that resulted from the current injection.

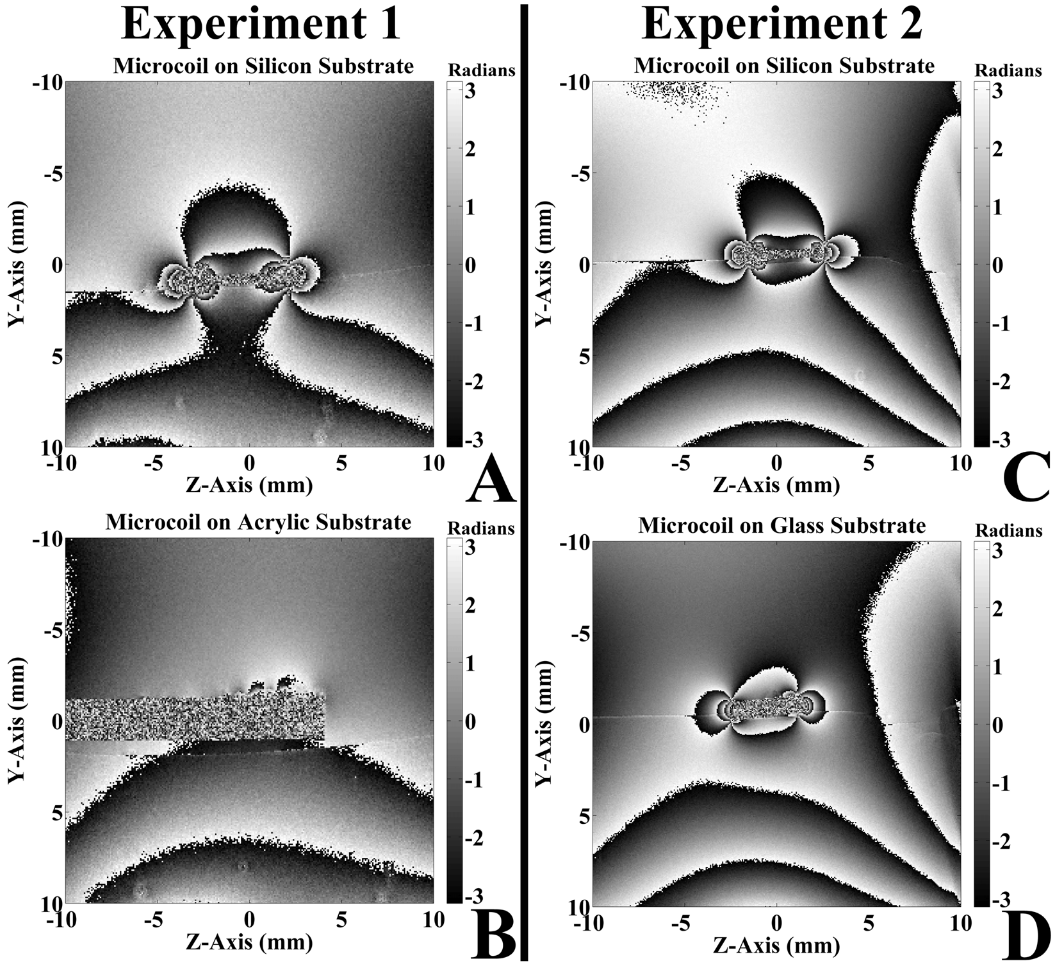

Figure 3-7 Phase Difference Maps: Phase difference maps were examined to determine the B_0 distortion created by the microcoil materials. In Experiment 1, the acrylic substrate had a magnetic susceptibility near water and, therefore, contributed no B_0 distortion. However, small B_0 distortions originated from the location of the fixed copper microcoil (B). Severe B_0 distortions originated from the silicon substrate (A), which was evident in the non-uniform phase measurements surrounding the substrate. In Experiment 2, a less severe, but significant, B_0 distortion was measured from the glass substrate (D) compared to the silicon (C).

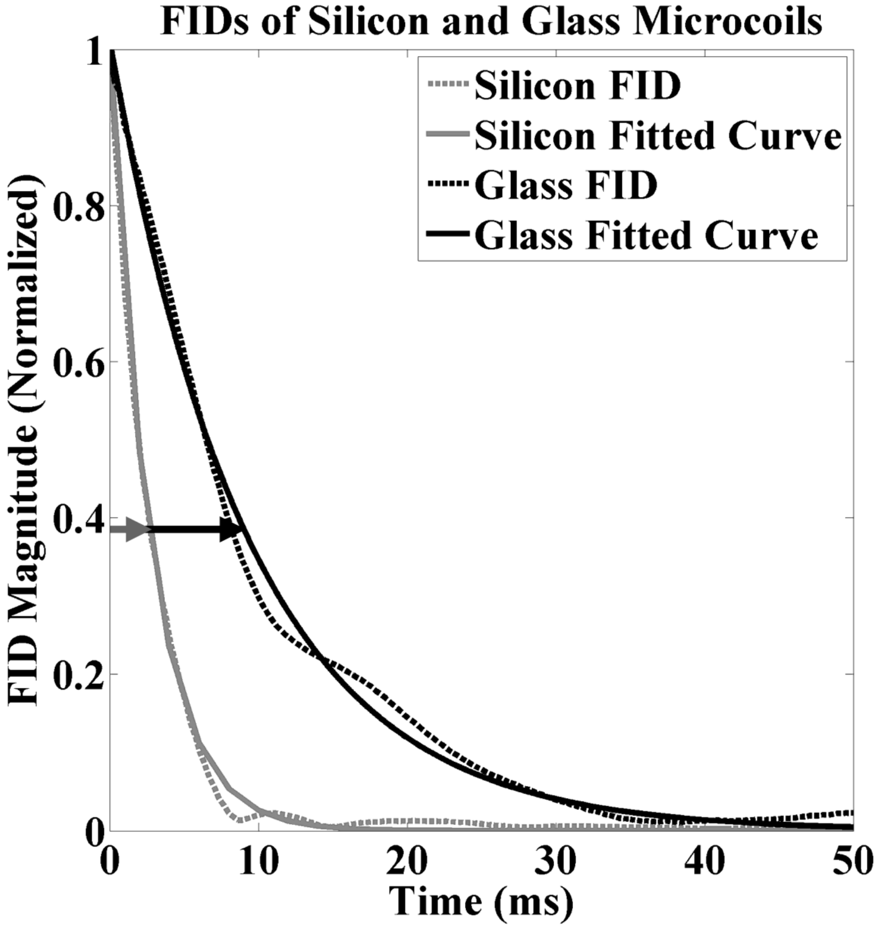

Figure 3-8 FIDs from Glass and Silicon Microcoils: Microcoils were manufactured on both silicon (gray lines) and glass substrates (black lines). FIDs were acquired from each microcoil type and the FID magnitude plotted in time. Exponential decay curves (solid lines) were fitted to the discretely measured FIDs (dashed lines) and the signal decay constant, T_2*, was calculated from each fitted curve. Representative measurements were chosen for the silicon and glass microcoil types. The T_2* was measured at 2.7 ms for the silicon (gray arrow) and 9.3 ms for the glass (black arrow). These results agree with the phase difference maps and show that the glass substrate distorted B_0 less than the silicon substrate. The glass microcoil had an adequate T_2* for application to the simultaneous hippocampal slice experiment.

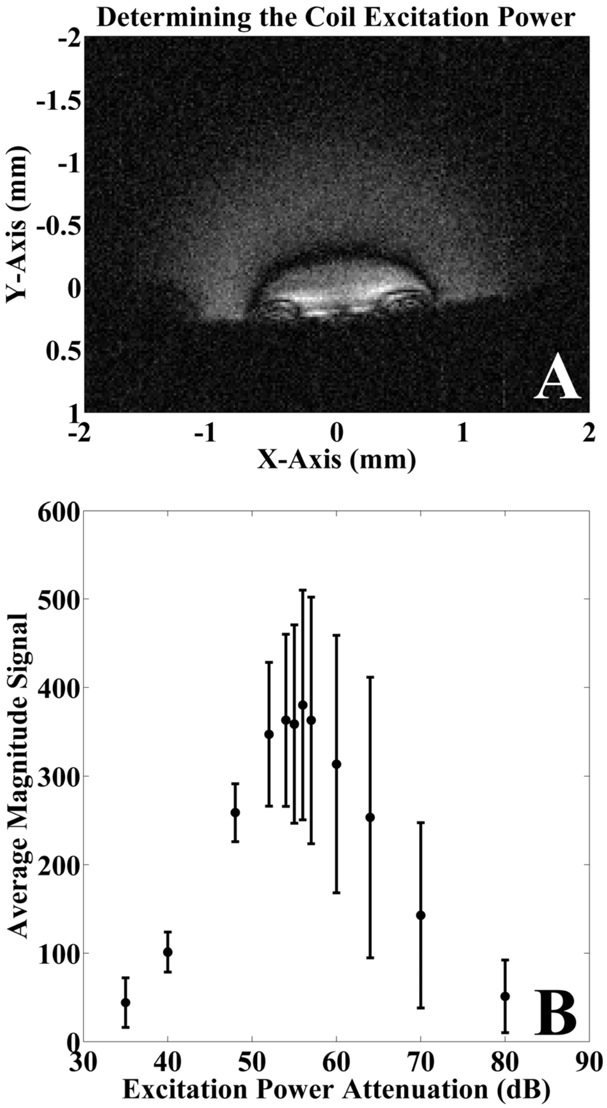

Figure 3-9 Determining the Microcoil Excitation Power: The excitation pulse transmission power was determined for the glass surface microcoil. The image in panel A shows an excessive transmission power (35 dB) that resulted in dark bands of no signal where the proton spins were excited out of the transverse plane (A). The goldilocks transmission power was determined by varying the excitation power attenuation and calculating the average magnitude signal in the area that the hippocampal slice occupied. A plot (*M* ± *SD*) revealed an attenuation value of 56 dB to be optimal (B).

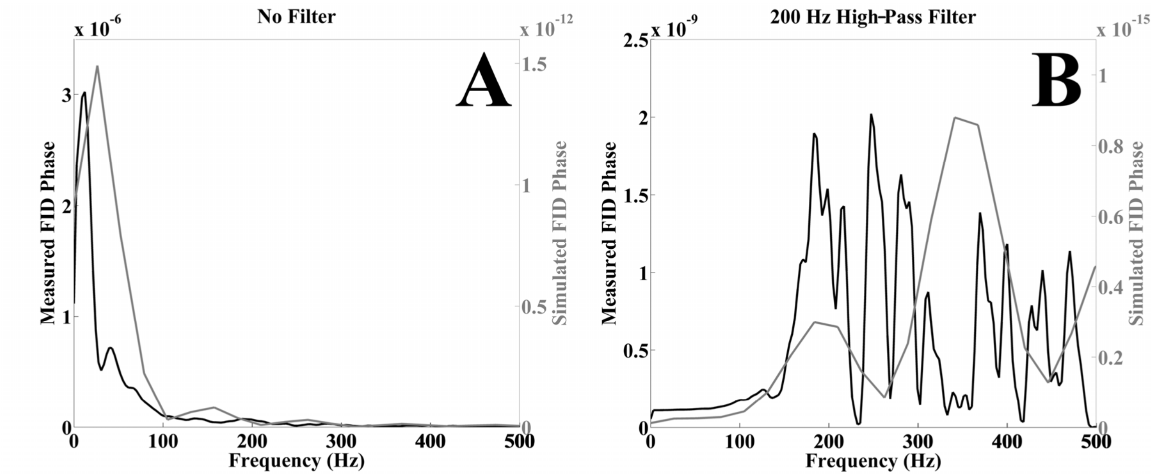

Figure 3-10 Spectral Densities of Theory and Experiment: The Welch power spectral densities for the measured and simulated FID phase time courses were estimated. The predicted FID phase time course from the evoked activity of a hippocampal CA1 volume (neuron type 2, z-orientation) was simulated by Cassarà, Hagberg et al. (2008).The frequency spectrum for this simulation (gray lines) was compared to the spectrum of the control FID phase measurement (black lines) of our experiment. This showed that the phase simulation and control phase measurement were dominated by low frequency components (0-100 Hz) (A). These frequencies were eliminated with the application of a 200 Hz, 4th order, Type 1 Chebyshev high-pass filter (B). The amplitude of the phase frequencies was greater in the measured FID than the simulated FID (NB: Y-axis scaling are different for each line).

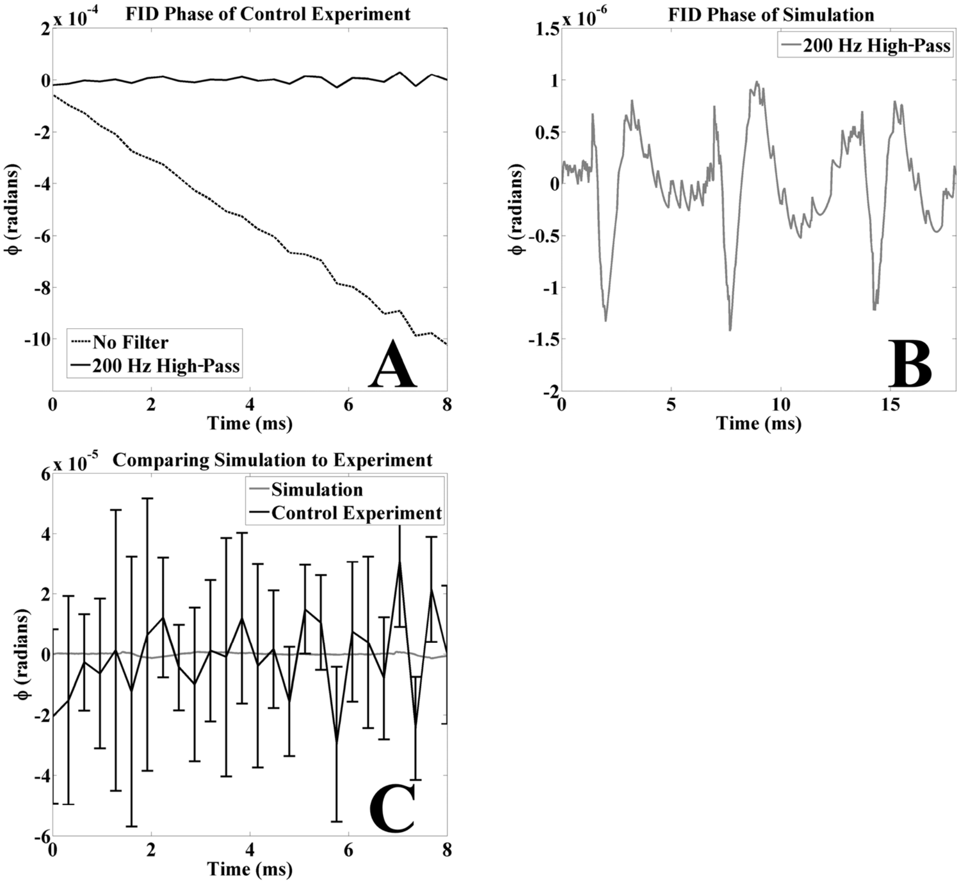

Figure 3-11 Comparing Theory and Experiment: The measured and simulated phase time courses were compared. Severe low-frequency drift was observed in the measured FID phase of the control time course (dashed black line). This agreed with the large 0-100 Hz component of the unfiltered frequency spectrum. A 200 Hz high-pass filter successfully removed this drift and stabilized the baseline (solid black line) (A). The 200 Hz high-pass filter was also applied to simulated phase time course of Cassarà, Hagberg et al. (2008) (solid gray line, neuron type 2, z-orientation) (B). A superimposition of the measured and simulated phase time courses (200 Hz high-pass filtered only) revealed that the simulated phase change was 25-100 times less than the detection threshold of our measured FID phase (C). The plot in panel C represents the mean radians ± SEM of 4,985 phase time courses.

3-5 Discussion

This study presents data demonstrating that the microcoil on glass substrate has superior FID characteristics (i.e., SNR and T_2*), compared to the microcoil on silicon substrate. In addition, the optimal transmission power for the microcoil was determined for the specific volume that the hippocampal slice occupied. However, the results of our simultaneous field potential recording and MRS experiment were unable to detect an evoked hippocampal event in the CA1 region of the rat hippocampus following stimulation of the Schaffer collaterals. The detection threshold of the control FID was 25-100 times greater than the phase change predicted by Cassarà, Hagberg et al. (2008) for a similar evoked event.

3-5.1 Silicon vs. Glass Microcoil Substrate. Two different microcoil substrates were examined to minimize the effects of the substrates magnetic susceptibility and to optimize the detectable signal of the FID. The first design of the RF microcoil contained a silicon substrate, which provided the structural platform for the copper coil traces. The epoxy and copper layers adhered well to the silicon substrate during the manufacturing process and always resulted in a functional microcoil. However, the average T_2* of the microcoil on the silicon substrate was 2.9 ms, which is significantly less than the estimated duration of an evoked hippocampal event (~10 ms). The detectable signal of the FID exponentially decays 63.2% following every evolution of T_2* and results in an incomplete capture of the hippocampal activity (Fig. 3-8). Therefore, a T_2* of 2.9 ms contains an estimated 3.2% of the original signal 10 ms after the RF excitation pulse. An increase of the FID signal decay time was necessary before proceeding with the simultaneous field potential recording and MRS experiment.

Phase difference maps of the microcoil on silicon substrate and the copper coil fixed to an acrylic wafer were examined to determine the source of the short T_2*. A phase difference map measures the magnetic field created by different materials exposed to a static magnetic field, such as B_0, and is defined by the magnetic susceptibility of the material. A difference between the magnetic susceptibility of the microcoil material and water distorts B_0 and causes the surrounding water protons to lose phase coherence. The loss of phase coherence causes the T_2* to decrease and results in a faster exponential decay of the detectable FID signal. Fig. 3-7 illustrates that the silicon substrate is the major source of magnetic field distortion (A), as the copper coil alone contributes significantly less distortion (B). The copper coil is fixed to an acrylic wafer, which is known to not distort B_0. The replacement of glass as the substrate material shows a smaller distortion in B_0 (D), compared to the same experiment with the original silicon substrate (C). The average T_2* of the microcoil on glass substrate was 9.0 ms (Fig. 3-8) and the remaining signal at the end of the 10-ms evoked hippocampal event was estimated to be 32.9% of the original signal following the RF excitation pulse. This ten times increase in the remaining signal at the end of the hippocampal activity is a sufficient increase for the simultaneous field potential recording and MRS experiment. In addition, a 2.8-times increase in the SNR was observed in the microcoil on glass substrate compared to the silicon.

The manufacturing process of the microcoil on the glass substrate was more difficult than the same process on the silicon substrate. The copper and epoxy layers did not adhere to the glass substrate well and, as a result, the majority of these coils were non-functional. Additionally, the microcoils that survived the manufacturing process would lose functionality after 3-12 hr of repeated transmission during the excitation pulse. These disadvantages of the glass substrate made manufacture and retention of the microcoil functionality difficult. However, the advantages of increased T_2^* and SNR gave a short window of opportunity to examine the average FID for a complete 5-6 hr simultaneous field potential recording and MRS experiment.

3-5.2 Determination of the Excitation Power. The power applied to the RF microcoil during the excitation pulse was optimized in the volume of the hippocampal slice. A determination of the excitation power is required because the location of the water proton signal changes as a function of transmission power. The FID is measured when the proton magnetization vector is excited from its steady-state orientation, parallel to B_0 (M_z), to an orientation in the plane transverse to B_0 (M_{xy}). This is accomplished by applying a RF excitation pulse at the resonant frequency from a transmission coil in the transverse plane. Once the excitation pulse is terminated, the magnetization vector freely rotates at the resonant frequency around the axis of B_0 and the component of the magnetization in the transverse plane (M_{xy}) induces a current in the receiving coil. The current induced in the receiving coil exponentially decays over time until the magnetization vector returns to its steady-state (M_z). The measurement of this current in the receiving coil is termed the FID. The single microcoil in our experiment was designed to both transmit and receive at the resonant frequency (400.3 MHz).

M_{xy} is the only component of the proton magnetization vector that contributes to the signal detected in the FID. Therefore, the transmission pulse must be precisely tuned to excite the magnetization vector only to the transverse plane. The detectable signal can be calculated from the sine of the excitation angle (θ) of the magnetization vector as it deviates from the steady-state:

$$M_{xy} = M_z \sin\theta \qquad \textbf{Eq. 3-5}$$

An excitation pulse with too much or too little power will result in a sub-optimal FID, as the excitation angle will be above or below $\pi/2$, respectively.

In addition, the transmission power of surface coils decays as the distance from the coil increases. In this way, an excitation angle gradient of the proton magnetization vector is observed as the distance increases from the microcoil surface. In Fig. 3-9A, θ is greatest on the surface of the microcoil and decreases as the distance from the microcoil center increases. Bright bands correspond to locations of maximal detectable signal ($\theta = \pi/2, 3\pi/2, 5\pi/2$, etc.), while dark bands correspond to locations of no detectable signal ($\theta = \pi, 2\pi, 3\pi$, etc.). The excitation pulse power was optimized by maximizing the detectable signal in the volume of the hippocampal slice. The magnitude signal in a 1.00 mm x 0.35 mm region immediately above the microcoil surface was measured and the average magnitude signal within this region was plotted at varying excitation powers. A parabola was observed with the excitation power at the peak corresponding to a maximal detectable signal and an optimal excitation power. In terms of the excitation angle, the sine of the average θ in the occupied region of the hippocampal slice is near 1 for optimal excitation, while excitation powers above and below the optimal power have an average value of less than 1. The optimal excitation power for each microcoil was determined before proceeding to the simultaneous field potential recording and MRS experiment.

3-5.3 Simultaneous Field Potential Recordings and MRS Following Evoked Activity in CA1. The simultaneous control experiment established the detection threshold of our methods. Evoked activity in the hippocampal slice was terminated by a brief application of $_{dd}H_2O$. The lack of field potentials was verified with simultaneous field potential recordings from the stratum pyramidale of the hippocampus CA1 region. Stimulation to the stratum radiatum, O_2 and CO_2 aeration, ACSF heating and ACSF perfusion were identical in the control and experimental conditions. The FID was acquired 0.1 ms after the slice was stimulated as shown in Fig. 3-5.

The average of 4,985 phase FID time courses was calculated and the Welch's power spectral density was estimated (Fig. 3-10A, black line). A large low-frequency component (0-100 Hz) dominated all other frequencies and was observed as a drift in the baseline of the time-domain FID phase (Fig. 3-11A, dashed black line). One source of the low-frequency component may be due to small instabilities in the static magnetic field that occur within a single T_R. Gross instabilities in the static magnetic field that occur beyond a single T_R were corrected during the post-processing of the FID data. Stimulation to the hippocampal slice occurs during even T_Rs, while there is no stimulation during odd T_Rs. The FID phase of a single odd T_R is subtracted from the FID phase of the subsequent even T_R to eliminate drifts in the phase that occur over a time greater than a single T_R. A second possible source of the low-frequency drift in the FID phase is the electrical stimulation to the hippocampal slice. The spreading current of the stimulation generates a magnetic field that can change the FID phase. The stimulation to the slice was terminated before the MRS excitation pulse to minimize the effects of the stimulating current on the MRS experiment. However, current flow is still possible following the cessation of the stimulating current and is evident in the stimulus artifact observed in evoked hippocampal slice field potential recordings (Fig. 3-6B, gray line). Such remnants of the tissue stimulation were not corrected by our post-processing methods and may account for the observed drift.

In addition, we observed a low-frequency component in the earthworm FID phase following a single evoked action potential. We applied a high-pass filter to the earthworm FID phase to eliminate the low-frequency drift that was required to observe the FID phase change associated with an evoked action potential. A similar 200 Hz high-pass filter was applied to the hippocampal FID phase. The low-frequency component in the Welch power spectral density estimate (Fig. 3-10B, black line) and the drift in the time-domain FID phase (Fig. 3-11A, black line) were both eliminated following the application of the filter.

3-5.4 Simulated Effects of Evoked CA1 Hippocampal Neuron Activity on the MR Signal. Cassarà, Hagberg et al. (2008) simulated the effect of evoked NMFs following the repeated stimulation of hippocampal CA1 neurons. The neurons were digitized representations of real CA1 pyramidal neurons with accurate morphologies and biophysical properties that were previously described (Migliore, Ferrante et al. 2005). The computer simulation predicted the electrical activity of a neuron volume and included realistic passive membrane properties and active voltage-gated conductances. Simulated pyramidal cell bodies were located to the center of a 1.7 mm^3 voxel. Effects of the MR magnitude and phase were calculated for different orientations of the neuron principal axis with respect to the external magnetic field (B_0). The neuron principal axis was defined as the line drawn parallel to the length of the neuron from the apical dendrites, through the neuron cell body and ending in the basal dendrites. Excitation to the CA1 volume was concentrated on the oblique dendrites in the stratum radiatum and represented excitatory connections from the Schaffer collaterals. Synapses were synchronously activated with AMPA-like excitatory input at a frequency of 154 Hz, which corresponded to a 6.5 ms period of repeating activity. Excitation to the oblique dendrites was designed to elicited action potential spikes from the CA1 neurons.

The MR signal changes were calculated for the 1.7 mm^3 volume, which contained the evoked magnetic fields of 3,600 neurons. Weaker magnetic fields originating from 14,162 neurons surrounding the volume were included in the simulation. The greatest MR magnitude and phase changes occurred when the neuron principal axis was transverse to B_0 (x- and z-orientations), while the least changes occurred when the neuron principal axis was parallel to B_0 (y-orientation). The magnetic field generated by a current carrying conductor is oriented perpendicular to the direction of current flow. Therefore, the dendrites and axons of neurons that are transverse to B_0 have a larger component of their neural magnetic fields oriented parallel to B_0. The component of the NMFs that is parallel to B_0 integrates with B_0 and causes a detectable MR signal change. Cassarà et al. (2008) reported the greatest MR signal change resulting from neurons that were oriented transverse to B_0. This finding is consistent with the theoretical detection of NMFs with MR technology.

The MR magnitude changes were predicted to be 100 times less than the changes associated with the MR phase (Cassarà, Hagberg et al. 2008). In addition, the predicted FID magnitude change was 10,000 times less than the predicted phase change associated with an earthworm action potential. Both simulations agree that the MR signal changes associated with the NMF are more detectable in the signal phase when compared to the MR magnitude change in the FID. For this reason, only the MR phase changes were considered. The maximum phase change associated with evoked activity in the CA1 volume resulted from a volume of CA1 pyramidal type 2 neurons with the principal axis of the neurons oriented in the z-direction (transverse to B_0). The phase change was determined at different echo times with a sampling interval of 25 μs between time points, compared to the current study that has a sampling interval of 320 μs. Therefore, the results of the Cassarà simulation are directly comparable to the current study because the former study has a finer temporal resolution that can be adjusted to the coarse resolution of our experiment. NMFs originating from the axons and dendrites contribute two different components to the simulated phase change. First, a slow, low-frequency drift is observed in the phase that changes Δ20 x 10^{-6} radians over the course of 20 ms. This slow component is attributed to NMFs originating from dendrite ligand-gated ion channels that concentrate current flow to a single net direction. Second, a fast, high-frequency component is observed to de-phase and re-phase at a period that matches the frequency of evoked activity in the simulation (6.5 ms). This component is attributed to the CA1 neuron action potential spikes, which have opposing sodium and potassium currents resulting in opposing NMFs that counteract the phase change.

The simulated phase change of the CA1 pyramidal type 2 neurons in the z-orientation was further analyzed in the frequency-domain using a Welch power spectral density estimate. The low-frequency component observed in the time-domain dominated all other frequencies from 0-100 Hz (Fig. 3-10A, gray line). This suggests that the NMFs attributed to the dendrites are the major source of MR phase change. This low-frequency component was successfully removed using a 200-Hz high-pass filter that was identical to the filter used on the FIDs in our experiment (Fig. 3-10B, gray line). The slow drift of the phase associated with the dendritic NMFs was removed in the time-domain, while the fast de-phasing and re-phasing components of the axonal NMFs remained (Fig. 3-11B). The theoretical de-phasing and re-phasing signature of the axonal NMFs calculated by Cassarà, Hagberg et al. (2008) is consistent with our previous observations that the phase change returns to baseline for a single evoked action potential in the earthworm (Fig. 2-4).

3-5.5 Comparing the Simultaneous Hippocampal Experiment to the Simulation in CA1 Pyramidal Neurons. The simultaneous field potential recording and MRS experiment in the hippocampal slice and the theoretical Cassarà simulation in CA1 pyramidal neurons are directly compared. First, hippocampal slices were harvested from rat brains to study the evoked NMFs of CA1 pyramidal neurons in our experiment. Cassarà, Hagberg et al. (2008) also studied CA1 pyramidal neurons that were digital reconstructions of CA1 neurons from the rat hippocampus. Second, we evoked activity from the CA1 neurons by stimulating the Schaffer collaterals. Similarly, the Cassarà simulation caused synchronous AMPA-like depolarization at 23 random locations of the oblique dendrites to mimic excitatory input from the Schaffer collaterals. The stimulation threshold of the experiment and the synchronous activation of dendrites in the Cassarà simulation were set to elicit a population action potential spike from the CA1 neurons. Third, MR sampling period of the Cassarà simulation (25 μs) was faster than our MR sampling period (320 μs). Therefore, the experimental and simulation phase time courses could be directly compared since the Cassarà simulation had a temporal resolution that was greater than our experimental methods.

A time window of 8 ms was chosen in the experimental and simulated phase time courses, since this time duration is less than the average T_2* of the acquired FID. This window ensures that each time point shown has 36% of the signal remaining after the RF excitation pulse. The majority of the phase change of the Cassarà simulation is from the low-frequency phase drift resulting from the dendritic currents. However, the phase drift contaminant observed in the control phase FID (Fig. 3-11A, dashed black line), following termination of CA1 activity with $_{dd}H_2O$ and verification with simultaneous field recordings, was greater than the simulated dendritic phase drift. Therefore, the low-frequency drift that contaminated the control FID concealed all changes that were a function of the dendritic NMFs.

The control FID phase was filtered with a 200 Hz high-pass filter to remove the low-frequency contaminant. The same 200 Hz high-pass filter must also be applied to the simulated phase change (Fig. 3-11B) to compare the two phase time series. The limits of detection for the control FID were 25-100 times above that of the predicted phase change (Fig. 3-11C). The experimental limits of detection make the recognition of neural magnetic fields impossible with the existing experimental methods in the hippocampal slice.

3-5.6 Inability to Detect Hippocampal NMFs and Future Directions. A comparison of our experimental detection limits and the theoretical simulation of Cassarà, Hagberg et al. (2008) provided evidence that detection of hippocampal NMFs were not possible with our current methods. Although there were many similarities between our experiment and the Cassarà simulation that allowed for direct comparison, there were differences between these studies that may further decrease the simulated phase change. First, the hippocampal neurons were stimulated at a frequency of 154 Hz and resulted in two complete excitations of the CA1 neurons in the 0-8 ms window defined by our T_2*. This high frequency of stimulation allowed for a continuous drifting of the phase as the magnetic field produced by the dendrites did not return to zero before the onset of the next stimulation. By stimulating one time, as in our experiment, it was expected that the phase would eventually reach a steady state at a non-zero phase since the generated magnetic fields return to zero. This would prevent the continuous drifting of the phase as observed in the Cassarà simulation. Next, the Cassarà simulation determined the MR signal change following the excitation of a 1.700 mm^3 volume of CA1 neurons. The maximum volume of our experiment was 0.275 mm^3, which is 16.2% of the simulated volume. The experimental volume of CA1 neurons was calculated by assuming that the CA1 neurons covered the entire sensitive region of the coil (0.785 mm^2), no CA1 neurons were damaged during the slice cutting process (0.350 mm slice thickness) and all CA1 neurons were evoked with a single stimulation of the Schaffer collaterals. The phase change produced by a volume of 16.2% of the simulated volume was expected to be much less than the Cassarà simulation because the net magnetic field produced by our experimental neural volume decreases with respect to the fewer accumulated NMFs of single neurons.

The major limitation to the simultaneous experiment was the SNR and T_2^* of the FID produced by the microcoil on glass substrate. Although improvements were made by substituting the silicon substrate with the glass, a further enhancement in the SNR and T_2^* can be expected if the substrate material matches the magnetic susceptibility of water. Plastics made from hydrocarbons are a good choice of material since their magnetic susceptibility is about the same as water. However, such a material will fail the microelectromechanical manufacturing processes used in the current study. A second possibility to improve the microcoil design is to remove the substrate from the microcoil after the manufacturing process. However, the removal of the substrate will subject the microcoil to mechanical stress and will cause the microcoil to become non-functional with little handling.

A new neural-tissue experimental model with a net NMF greater than the evoked hippocampal slice is necessary to increase the MR detectability of neural electrophysiology. Attributes of the hippocampal slice model, such as morphology and electrophysiology, should be considered for application to other neural systems. The morphology of the CA1 neurons are oriented in a single direction. This permits the neurons to be aligned in an orientation transverse to B_0 and allows for a maximum change in the MR signal to be achieved. The electrophysiology of the hippocampal slice is well known. Stimulation of the Schaffer collaterals elicits synchronous activity from the CA1 neurons. Synchronous activity permits a greater accumulation of individual NMFs in time and results in a greater net NMF. The new experimental model should also compensate for the disadvantages of the hippocampal slice that decrease MR detectability. The hippocampal slice cannot exceed a certain thickness before nutrient delivery and waste removal is insufficient to sustain neuron viability. Therefore, the volume of the neural tissue is severely limited and results in a smaller net NMF. The bloodless turtle brain was used in another similar study and has the benefit of a larger neuron volume (Luo, Lu et al. 2009). A different experimental model that incorporates the advantages and removes the disadvantages of the hippocampal slice model may increase the detectability of the NMF with MR technology.

3-6 Conclusion

The direct detection of NMFs from evoked CA1 neurons of the rat hippocampal slice was not possible under the current experimental conditions. The detection limits of our experiment, determined by the time course of the control FID phase, is 25-100 times above the predicted phase changes by Cassarà, Hagberg et al. (2008). Our experimental techniques were optimized to increase the sensitivity of our methods and to detect very small changes in the MR signal. The direct measurement of NMFs in the hippocampal slice is impractical since even under optimal conditions, NMFs have a minor effect on the MR signal. Further technological advancements and increased sensitivity to minute changes in the static magnetic field are required for future studies investigating the direct detection of NMFs with MRS technology.

CHAPTER 4

Conclusions and Future Directions

4-1 Conclusions

Our studies examined the direct detection of neural magnetic fields (NMFs) with magnetic resonance (MR) technology in the absence of the hemodynamic response. Simultaneous local field potentials and magnetic resonance spectroscopy (MRS) were used to capture single evoked events and to examine the effects of NMFs on the sub-millisecond temporal resolution free-induction decay (FID).

A single axonal NMF was successfully detected in the median giant fiber of the earthworm. Evoked action potentials were time-locked to the start of the FID acquisition and compared to FIDs in the absence of action potentials. We observed a change in the FID phase, and not the FID magnitude, that agreed with the theoretically simulated phase change of a volume conductor model adaptation (Roth and Wikswo 1985; Woosley, Roth et al. 1985).

Detection of a single evoked event in the CA1 region of the rat hippocampal slice was impossible with the current experimental methods. Activity in the hippocampal slice was permanently terminated in the control condition and FIDs were acquired 1 ms after stimulation of the Schaffer collaterals in order to assess the detection limits of our experiment. The conditions of the control experiment included perfusion of the artificial cerebral spinal fluid (ACSF), heated ACSF, 95% O_2 and 5% CO_2 ACSF aeration, stimulation of the Schaffer collaterals and recording at the CA1 stratum pyramidale. The detection limits were determined to be 25-100 times above the predicted phase change that was determined for a similar volume of evoked CA1 neurons (Cassarà, Hagberg et al. 2008).

We believe that the major discrepancy between our two findings indicate that our methods are more sensitive to axonal magnetic fields than dendritic magnetic fields.

Axonal magnetic fields are generated by two opposing ionic currents. First, inward sodium currents, which flow through voltage-gated sodium channels located in the axon cell membrane, are responsible for the initial depolarizing component of the action potential. These voltage-gated sodium channels rapidly inactivate and prevent further influx of sodium ions. The magnetic field that results from this ionic current shifts the FID phase signal in a negative direction. Voltage-gated potassium channels open near to the time that the sodium channels inactivate and create an outward flux of potassium ions. The current attributed to the potassium ions generates a magnetic field that opposes the sodium current and shifts the FID phase signal in a positive direction. These opposing phase shifts caused by the sodium and potassium currents occurs within 1-2 ms and returns the phase to its original baseline at the completion of the action potential event. In this way, axons contribute a high-frequency component (>100 Hz) to the FID time course.

On the other hand, dendritic magnetic fields are associated with a slower and longer lasting current flux that is concentrated to a single net direction of flow through ligand-gated ion channels. The current through these channels causes the FID phase to shift in a single direction (positive or negative) that continues as long as the channels are open. No opposing dendritic FID phase shift is observed because a concentrated current flow in the opposite direction does not localize at the ligand-gated channels. Therefore, the FID phase settles at a new steady-state that is not the original baseline and contributes a low-frequency component (<100 Hz) to the FID time course.

In addition, the FID phase time course of our experiments contains a low-frequency contamination that does not result from neural activity. The low-frequency component (<100 Hz) is dominant in the control FID phase in both the earthworm and rat hippocampal slice experiments when evoked activity is not present. The source of the low-frequency component is most likely due to remnants of the tissue stimulation or to small instabilities in the static magnetic field of the magnet. However, the low-frequency component contaminates the FID phase and completely obscures the small MR signal changes associated with the NMFs. A high-pass filter is necessary to remove the low-frequency contaminant of the FID phase and, subsequently, eliminates the low-frequency phase change associated with dendritic NMFs. Therefore, only the axonal NMFs are detectable with our methods as the axon phase signature does not contain frequencies that overlap with the low-frequency contamination.

4-2 Future Directions

The measurement of evoked NMFs by the direct examination of the FID phase is currently limited to the magnetic fields of axons and not to dendrites. Our study successfully detected a single evoked action potential in an invertebrate model. Future directions should continue with *in vitro* studies since the hemodynamic response to axonal activation in white matter is not completely understood. In addition, the FID phase change associated with the activation of multiple axons in a nerve fiber is more applicable to axon function in mammals.

The *in vitro* rat sciatic nerve is proposed for the next step in the study of axon magnetic fields with our methods.

The rat sciatic nerve is a large fiber bundle located in the hind limb of the rat and contains afferent and efferent axons. The main sciatic trunk can be dissected from the thigh at the sciatic notch to the knee. The sciatic trunk is composed of the tibial, peroneal, sural and posterior cutaneous nerves that separate at the knee to innervate different targets of the lower hind limbs. The sciatic nerve contains axons of alpha- and gamma-efferent motoneuron and types I-IV afferent sensory neurons. Axon diameter, myelination and action potential conduction velocity vary for each of these axon types and activation of the entire sciatic nerve would create a conglomerate of generated axon magnetic fields. In this way, the NMF generated by the sciatic nerve represents a good model for the study of *in vivo* human white matter activation.

The experiment in the rat sciatic nerve will share aspects of the earthworm experiment. The sciatic nerve can be drawn through the center of a solenoid microcoil and be located in the most sensitive region of the coil. Changes in the FID phase can be measured at a sub-millisecond temporal resolution using similar MRS methodology. In addition, electrical stimulation of the sciatic nerve generates thousands of action potentials and simultaneous field potential recordings at the entrance and exit of the microcoil can determine the population conduction velocity. Sciatic axons are asymmetrically distributed within the four sub-nerves and common types of axons are anatomically grouped within distinct regions of the nerve (Swett, Wikholm et al. 1986; Badia, Pascual-Font et al.

2010). Activation of a select axon type will generate an asymmetric NMF that will increase its detectability in the FID.

Possible challenges for the *in vitro* rat sciatic nerve experiment include perfusion of ACSF containing paramagnetic oxygen gas and the unknown longevity of the sciatic nerve. Oxygen gas is a paramagnetic compound that generates a magnetic field that strongly opposes B_0. Local introduction of oxygen gas in the physiological saline will create an MR phase and magnitude change (Luo, Liu et al. 2007) that may mask signal changes originating from the nerve. The earthworm nerve cord did not require ACSF perfusion or dissolved oxygen gas to maintain neural activity. However, the rat sciatic nerve requires oxygen gas to preserve its function. A theoretical estimate on the effects of dissolved oxygen gas on the FID is required to determine if it will contribute more MR signal changes than the sciatic nerve NMF. In addition, the longevity of sciatic nerve and the amount of time it can sustain activation is unknown. 7-10 hr were required for each earthworm to obtain enough repetitions (one stimulation every 4 s). If the *in vitro* rat sciatic nerve can produce action potentials during a similar time requirement, then identification of the sciatic NMF in the FID may be possible.

Recent applications of optogenetics to evoke activity of the mouse sciatic nerve without the use of current stimulation can alleviate a possible source of confound in the earthworm study. The injection of electrical current to evoke action potentials generates a magnetic field that can be detected in the FID. However, photo-sensitive ion channels can be genetically inserted in the axon membrane and replace the use of current to evoke action potentials. For example, channel-rhodopsin-2 (ChR2) will activate after a brief pulse of light and open to allow cations through the axon membrane. The influx of cations depolarizes the axon and triggers an action potential. Activation of the mouse sciatic nerve with these photo-sensitive ion channels was shown without the application of exogenous current (Llewellyn, Thompson et al. 2010). Action potential generation using photo-sensitive methods will eliminate any source of FID signal change that may interfere with axonal NMF detection. The *in vitro* rat sciatic nerve is a potential next step in the identification of axon NMFs since it includes synchronized activation of thousands of action potentials in a mammalian system and is similar to *in vivo* human white matter function without the hemodynamic response

The direct detection of NMFs by examining the sub-millisecond FID is limited to axonal NMFs in our methods. Existing functional magnetic resonance imaging methods measure signal changes associated with neural activity within the gray matter and not the white matter. Currently, a method does not exist that measures MR signal changes that result from the functioning of white matter. In this way, the direct detection of axonal NMFs with our methods provides a new measure of functional neural imaging that is unlike current fMRI methods.

REFERENCES

Badia J, Pascual-Font A, Vivó M, Udina E and Navarro X (2010). *Topographical distribution of motor fascicles in the sciatic-tibial nerve of the rat*. Muscle Nerve **42**(2): 192-201.

Bianciardi M, Di Russo F, Aprile T, Maraviglia B and Hagberg GE (2004). *Combination of BOLD-fMRI and VEP recordings for spin-echo MRI detection of primary magnetic effects caused by neuronal currents*. Magn Reson Imaging **22**(10): 1429-1440.

Blagoev KB, Mihaila B, Travis BJ, Alexandrov LB, Bishop AR, Ranken D, Posse S, Gasparovic C, Mayer A, Aine CJ, Ulbert I, Morita M, Muller W, Connor J and Halgren E (2007). *Modelling the magnetic signature of neuronal tissue*. NeuroImage **37**(1): 137-148.

Bodurka J and Bandettini PA (2002). *Toward direct mapping of neuronal activity: MRI detection of ultraweak, transient magnetic field changes*. Magn Reson Med **47**(6): 1052-1058.

Bodurka J, Jesmanowicz A, Hyde JS, Xu H, Estkowski L and Li SJ (1999). *Current-Induced Magnetic Resonance Phase Imaging*. J Magn Reson **137**(1): 265-271.

Bortolotto ZA, Anderson WW, Isaac JTR and Collingridge GL (2001). *Synaptic Plasticity in the Hippocampal Slice Preparation*. Current Protocols in Neuroscience, John Wiley & Sons, Inc.**:** 6.13.11-16.13.23.

Bullock TH (1965). *Annelida*. Structure and Function in the Nervous Systems of Invertebrates. T. H. Bullock and G. A. Horridge. San Francisco, W. H. Freeman and Company. **I:** 661-789.

Buxton RB and Frank LR (1997). *A Model for the Coupling Between Cerebral Blood Flow and Oxygen Metabolism During Neural Stimulation*. J Cerebr Blood F Met **17**(1): 64-72.

Cassarà AM, Hagberg GE, Bianciardi M, Migliore M and Maraviglia B (2008). *Realistic simulations of neuronal activity: A contribution to the debate on direct detection of neuronal currents by MRI*. NeuroImage **39**(1): 87-106.

Chow LS, Cook GG, Whitby E and Paley MNJ (2006). *Investigating direct detection of axon firing in the adult human optic nerve using MRI*. NeuroImage **30**(3): 835-846.

Chow LS, Cook GG, Whitby E and Paley MNJ (2006). *Investigation of MR signal modulation due to magnetic fields from neuronal currents in the adult human optic nerve and visual cortex*. Magn Reson Imaging **24**(6): 681-691.

Chow LS, Cook GG, Whitby E and Paley MNJ (2007). *Investigation of axonal magnetic fields in the human corpus callosum using visual stimulation based on MR signal modulation*. J Magn Reson Imaging **26**(2): 265-273.

Chow LS, Dagens A, Fu Y, Cook GG and Paley MN (2008). *Comparison of BOLD and direct-MR neuronal detection (DND) in the human visual cortex at 3T*. Magn Reson Med **60**(5): 1147-1154.

Chu R, de Zwart JA, van Gelderen P, Fukunaga M, Kellman P, Holroyd T and Duyn JH (2004). *Hunting for neuronal currents: absence of rapid MRI* *signal changes during visual-evoked response*. NeuroImage **23**(3): 1059-1067.

Drewes C, Landa K and McFall J (1978). *Giant nerve fibre activity in intact, freely moving earthworms*. J Exp Biol **72**(1): 217-227.

Drewes CD (1984). *Escape Reflexes in Earthworms and Other Annelids*. Neural Mechanisms of Startle Behavior. R. C. Eaton. New York, NY, Plenum Press**:** 43-91.

Drewes CD and Pax RA (1974). *Neuromuscular physiology of the longitudinal muscle of the earthworm, Lumbricus Terrestris. I. Effects of different physiological salines*. J Exp Biol **60**: 445-452.

Ehrmann K, Gersbach M, Pascoal P, Vincent F, Massin C, Stamou D, Besse PA, Vogel H and Popovic RS (2006). *Sample patterning on NMR surface microcoils*. J Magn Reson **178**(1): 96-105.

Ernst T and Hennig J (1994). *Observation of a Fast Response in Functional MR*. Magn Reson Med **32**(1): 146-149.

Eroglu S, Gimi B, Roman B, Friedman G and Magin RL (2003). *NMR spiral surface microcoils: Design, fabrication, and imaging*. Concepts Magn Reson, Part B **17B**(1): 1-10.

Gunther J (1976). *Impulse conduction in the myelinated giant fibers of the earthworm. Structure and function of the dorsal nodes in the median giant fiber*. J Comp Neurol **168**(4): 505-531.

Haacke EM, Brown RW, Thompson MR and Venkatesan R (1999). Magnetic Resonance Imaging: Physical Principles and Sequence Design. New York, John Wiley & Sons, Inc.

Hagberg GE, Bianciardi M and Maraviglia B (2006). *Challenges for detection of neuronal currents by MRI*. Magn Reson Imaging **24**(4): 483-493.

Hämäläinen M, Hari R, Ilmoniemi RJ, Knuutila J and Lounasmaa OV (1993). *Magnetoencephalography - theory, instrumentation, and applications to noninvasive studies of the working human brain*. Rev Mod Phys **65**(2): 413.

Heller L, Barrowes BE and George JS (2009). *Modeling direct effects of neural current on MRI*. Hum Brain Mapp **30**(1): 1-12.

Herrault F, Chang-Hyeon J and Allen MG (2008). *Ultraminiaturized High-Speed Permanent-Magnet Generators for Milliwatt-Level Power Generation*. J Microelectromech S **17**(6): 1376-1387.

Herrault F, Yorish S, Crittenden TM, Ji CH and Allen MG (2010). *Parylene-Insulated Ultradense Microfabricated Coils*. J Microelectromech S **19**(6): 1277-1283.

Hillman H (2000). *Limitations of clinical and biological histology*. Med Hypotheses **54**(4): 553-564.

Huang R, Posnansky O, Celik A, Oros-Peusquens A-M, Ermer V, Irkens M, Wegener H-P and Shah NJ (2006). *Measurement of weak electric currents in copper wire phantoms using MRI: influence of susceptibility enhancement*. Magnetic Resonance Materials in Physics, Biology and Medicine **19**(3): 124-133.

Jasanoff A (2007). *Bloodless fMRI*. Trends in Neurosciences **30**(11): 603-610.

Jezzard P, Matthews PM and Smith SM, Eds. (2001). <u>Functional MRI: an introduction to methods</u>. New York, Oxford University Press Inc.

Kao CY and Grundfest H (1957). *Postsynaptic Electrogenesis in Septate Giant Axons. I. Earthworm Median Giant Axon*. J Neurophysiol **20**: 553-573.

Konn D, Gowland P and Bowtell R (2003). *MRI detection of weak magnetic fields due to an extended current dipole in a conducting sphere: A model for direct detection of neuronal currents in the brain*. Magn Reson Med **50**(1): 40-49.

Konn D, Leach S, Gowland P and Bowtell R (2004). *Initial attempts at directly detecting alpha wave activity in the brain using MRI*. Magn Reson Med **22**(10): 1413-1427.

Liston AD, Salek-Haddadi A, Kiebel SJ, Hamandi K, Turner R and Lemieux L (2004). *The MR detection of neuronal depolarization during 3-Hz spike-and-wave complexes in generalized epilepsy*. Magn Reson Imaging **22**(10): 1441-1444.

Llewellyn ME, Thompson KR, Deisseroth K and Delp SL (2010). *Orderly recruitment of motor units under optical control in vivo*. Nat Med **16**(10): 1161-1165.

Luo Q, Liu H-L, Parris B, Lu H, Senseman DM and Gao J-H (2007). *Modeling oxygen effects in tissue-preparation neuronal-current MRI*. Magn Reson Med **58**(2): 407-412.

Luo Q, Lu H, Lu H, Senseman D, Worsley K, Yang Y and Gao J-H (2009). *Physiologically evoked neuronal current MRI in a bloodless turtle brain: Detectable or not?* NeuroImage **47**(4): 1268-1276.

Madison D and Edson EB (1997). *Preparation of Hippocampal Brain Slices*. Current Protocols in Neuroscience, John Wiley & Sons, Inc.**:** 6.4.1-6.4.7.

Malonek D, Dirnagl U, Lindauer U, Yamada K, Kanno I and Grinvald A (1997). *Vascular imprints of neuronal activity: Relationships between the dynamics of cortical blood flow, oxygenation, and volume changes following sensory stimulation*. Proc Natl Acad Sci USA **94**(26): 14826-14831.

Massin C, Boero G, Vincent F, Abenhaim J, Besse PA and Popovic RS (2002). *High-Q factor RF planar microcoils for micro-scale NMR spectroscopy*. Sens Actuators, A **97-98**: 280-288.

Massin C, Vincent F, Homsy A, Ehrmann K, Boero G, Besse PA, Daridon A, Verpoorte E, de Rooij NF and Popovic RS (2003). *Planar microcoil-based microfluidic NMR probes*. J Magn Reson **164**(2): 242-255.

McFall JL, Landa KB and Drewes CD (1977). *Parameters of giant fiber conduction in intact, freely moving earthworms*. Am Zool **17**: 876.

Migliore M, Ferrante M and Ascoli GA (2005). *Signal Propagation in Oblique Dendrites of CA1 Pyramidal Cells*. J Neurophysiol **94**(6): 4145-4155.

Minard KR and Wind RA (2001). *Solenoidal microcoil design. Part I: Optimizing RF homogeneity and coil dimensions*. Concepts Magn Reson **13**(2): 128-142.

Minard KR and Wind RA (2001). *Solenoidal microcoil design. Part II: Optimizing winding parameters for maximum signal-to-noise performance*. Concepts Magn Reson **13**(3): 190-210.

Murakami S and Okada Y (2006). *Contributions of principal neocortical neurons to magnetoencephalography and electroencephalography signals*. J Physiol **575**(3): 925-936.

O'Gara B, Vining EP and Drewes CD (1982). *Electrophysiological correlates of rapid escape reflexes in intact earthworms, Eisenia foetida. I. Functional development of giant nerve fibers during embryonic and postembryonic periods*. J Neurobiol **13**(4): 337-353.

Ogawa S, Lee TM, Kay AR and Tank DW (1990). *Brain Magnetic Resonance Imaging with Contrast Dependent on Blood Oxygenation*. Proc Natl Acad Sci USA **87**(24): 9868-9872.

Okada YC, Wu J and Kyuhou S (1997). *Genesis of MEG signals in a mammalian CNS structure*. Electroencephalogr Clin Neurophysiol **103**(4): 474-485.

Park TS and Lee SY (2007). *Effects of neuronal magnetic fields on MRI: Numerical analysis with axon and dendrite models*. NeuroImage **35**(2): 531-538.

Park TS, Lee SY, Park J-H, Cho MH and Lee SY (2006). *Observation of the fast response of a magnetic resonance signal to neuronal activity: a snail ganglia study*. Physiol Meas **27**(2): 181-190.

Park TS, Lee SY, Park J-H and Lee SY (2004). *Effect of nerve cell currents on MRI images in snail ganglia*. NeuroReport **15**(18): 2783-2786.

Parkes LM, de Lange FP, Fries P, Toni I and Norris DG (2007). *Inability to directly detect magnetic field changes associated with neuronal activity*. Magn Reson Med **57**(2): 411-416.

Pell GS, Abbott DF, Fleming SW, Prichard JW and Jackson GD (2006). *Further steps toward direct magnetic resonance (MR) imaging detection of neural action currents: Optimization of MR sensitivity to transient and weak currents in a conductor*. Magn Reson Med **55**(5): 1038-1046.

Petridou N, Plenz D, Silva AC, Loew M, Bodurka J and Bandettini PA (2006). *Direct magnetic resonance detection of neuronal electrical activity*. Proc Natl Acad Sci USA **103**(43): 16015-16020.

Reid KH, Edmonds HL, Schurr A, Tseng MT and West CA (1988). *Pitfalls in the use of brain slices*. Prog Neurobiol **31**(1): 1-18.

Roberts MBV (1962). *The Giant Fibre Reflex of the Earthworm, Lumbricus Terrestris L., I. The Rapid Response*. J Exp Biol **39**(2): 219-227.

Ross KFA (1953). *Cell shrinkage caused by fixatives and paraffin-wax embedding in ordinary cytological preparations*. Q J Microsc Sci **94**(26): 125-139.

Roth BJ and Wikswo JP, Jr. (1985). *The magnetic field of a single axon. A comparison of theory and experiment*. Biophys J **48**(1): 93-109.

Rushton WAH (1946). *Reflex conduction in the giant fibres of the earthworm*. Proc R Soc London, Ser B **133**(870): 109-120.

Song AW and Takahashi AM (2001). *Lorentz effect imaging*. Magn Reson Imaging **19**(6): 763-767.

Swett JE, Wikholm RP, Blanks RHI, Swett AL and Conley LC (1986). *Motoneurons of the rat sciatic nerve*. Exp Neurol **93**(1): 227-252.

Swinney KR and John P. Wikswo J (1980). *A calculation of the magnetic field of a nerve action potential*. Biophys J **32**: 719-732.

Truong T-K, Avram A and Song AW (2008). *Lorentz effect imaging of ionic currents in solution*. J Magn Reson **191**(1): 93-99.

Truong T-K and Song AW (2006). *Finding neuroelectric activity under magnetic-field oscillations (NAMO) with magnetic resonance imaging in vivo*. Proc Natl Acad Sci USA **103**(33): 12598-12601.

Truong T-K, Wilbur JL and Song AW (2006). *Synchronized detection of minute electrical currents with MRI using Lorentz effect imaging*. J Magn Reson **179**: 85-91.

Webb AG (2005). *Microcoil nuclear magnetic resonance spectroscopy*. J Pharm Biomed Anal **38**(5): 892-903.

Wikswo JP (1989). *Biomagnetic sources and their models*. Advances in Biomagnetism. S. J. Williamson, M. Hoke, G. Stroink and M. Kotani. New York, Plenum Press**:** 1-18.

Woosley JK, Roth BJ and Wikswo JP (1985). *The magnetic field of a single axon: A volume conductor model*. Math Biosci **76**(1): 1-36.

Xiong J, Fox PT and Gao J-H (2003). *Directly mapping magnetic field effects of neuronal activity by magnetic resonance imaging*. Hum Brain Mapp **20**(1): 41-49.

Xue Y, Gao J-H and Xiong J (2006). *Direct MRI detection of neuronal magnetic fields in the brain: Theoretical modeling*. NeuroImage **31**(2): 550-559.